Chapter

# 8

# Sea Ice Monitoring by Remote Sensing

Authors: Stein Sandven and Ola M. Johannessen

## 8.1 INTRODUCTION

### 8.1.1 The Role of Sea Ice in the Climate and Weather System

Sea ice is a part of the cryosphere that interacts continuously with the underlying oceans and the overlaying atmosphere. The growth and decay of sea ice occur on a seasonal cycle at the surface of the ocean at high latitudes. As much as 30 million km$^2$ of the Earth's surface can be covered by sea ice. In the Northern Hemisphere, sea ice extent fluctuates each year from a minimum in September, when most of the ice is confined to the central Arctic Ocean, Greenland Sea and Canadian Archipelago, to a maximum in March, when the ice covers almost the entire Arctic Ocean and many adjacent seas. In the Southern Hemisphere, the annual fluctuation is even greater, from a minimum in February to a maximum in September when the ice surrounds the Antarctic continent and extends equatorward to 55°–65° S (Gloersen et al. 1992). Figure 8-1 shows an example of maximum and minimum ice extent obtained from passive microwave satellite data.

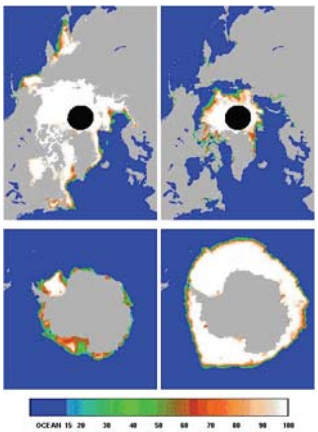


Figure 8-1 Maps of maximum and minimum sea ice extent and concentration in the Arctic (top) and Antarctic (bottom) obtained from passive microwave satellite data from the Special Sensor Microwave Imager (SSM/I). The maps are from March 1993 (upper left and lower left) and September 1993 (upper right and lower right). Ice concentrations, expressed as percent coverage and indicated by the color bar, were computed from SSM/I data using the Norwegian NORSEX algorithm. Courtesy: NERSC.

The largest volume of sea ice is found in the Northern Hemisphere in March, 0.05 million $km^3$, which is nearly twice the maximum sea ice volume in the Southern Hemisphere. The reason for this is that the mean thickness of Arctic sea ice is about 3 m, whereas the mean thickness of Antarctic sea ice is 1.0–1.5 m.

Sea ice research and monitoring is important for many countries at high latitudes, and also those who operate in Antarctica. Sea ice imposes severe restrictions on ship traffic in the Arctic. It is a sensitive climate indicator, and plays an important role in exploration and exploitation of marine resources. Sea ice has many roles in the global climate system. It serves as an effective insulator between the ocean and the atmosphere, restricting exchange of heat, mass, momentum and chemical constituents. During winter when there is a large temperature difference between the cold atmosphere and the relatively warm ocean surface, ocean-to-atmosphere heat transfer is essentially limited to areas of open water and thin ice within the pack. The winter flux of oceanic heat to the atmosphere from open water can be two orders of magnitude larger than the heat flux through an adjacent thick ice cover. As a result, the distribution of open water and thin ice is particularly important to the regional heat balance.

Another important role of sea ice in the global climate system is that it affects surface albedo. Ice-free ocean generally has an albedo below 10–15%, whereas snow-covered sea ice albedos average about 80%. A fresh snow cover on ice can increase the surface albedos to values as high as 98%, whereas melt ponds can decrease the ice albedos to as low as 20%. Because the albedo of snow-covered sea ice is high relative to that of open water, the presence of sea ice considerably reduces the amount of solar radiation absorbed at the Earth's surface. This is most significant in summer when the insolation, or solar heating, is high.

Sea ice processes also affect oceanic circulation directly by the rejection of salt to the underlying ocean during ice growth. This increases the density of the water directly under the ice, thereby inducing convection that tends to deepen the mixed layer. This convection contributes to driving the thermohaline circulation of the ocean and, in regions with density structures that were initially weak or unstable, can lead to overturning and deep water formation. Much of the world oceans' deep and bottom water is believed to be formed in polar latitudes by these mechanisms. Conversely, the input of relatively fresh water to the ocean during ice melt periods tends to increase the stability of the upper layer of the ocean, inhibiting convection. Furthermore, the net equatorward transport of ice in each hemisphere produces a positive freshwater transport and a negative heat transport.

On a hemispheric scale, the seasonal variability of ice extent and ice edge location is controlled by atmospheric and oceanic forcing, which include ocean temperature and salinity and atmospheric temperature and winds. The location of the ice edge will in turn feed back on several atmospheric and oceanic processes that affect the regional weather, such as generation of polar lows. On a regional scale, surface roughness of the ice and the drag coefficient depend upon ridging and rafting, both of which can be produced by wind- or wave-induced ice convergence. Ice observation is therefore important for weather forecasts at high latitudes.

Data from polar-orbiting satellites are used extensively in research, as well as for monitoring sea ice extent and other ice parameters (e.g., Johannessen et al. 1992, 1995, 1999, 2005; Jackson and Apel 2004). Large-scale ice drift can be estimated from passive microwave data (Kwok et al. 1998; Liu and Cavalieri 1998; Martin and Augstein 2000) and from scatterometer data (Zhao et al. 2002), while ice deformation and ice growth can be derived from systematic SAR coverage (Kwok et al. 1995; Kwok and Cunningham 2002). Ice thickness, another important ice parameter, has been difficult to measure accurately by spaceborne instruments (Wadhams 1994), but new methods using radar altimeters are under development (Laxon et al. 2003). One of the key objectives in sea ice science is to achieve the

capability of synoptically measuring sea ice thickness in both hemispheres. Data on ice thickness are very sparse, especially in the Antarctic. Present estimates of sea ice volume, which are mainly based on model results due to lack of data, can have errors of ± 50%. In the Arctic there are some synoptic surveys of ice thickness obtained by submarine sonar over the last four decades (Rothrock et al. 1999) and point measurements from expeditions and drifting ice stations. The data sets available provide some information about regional and seasonal variability, but are too sparse to provide a coherent picture.

General circulation models predict enhanced climatic warming in polar areas, and this is expected to be reflected in a reduced sea ice area and a decreased mean sea ice thickness (Johannessen et al. 2004). Only a satellite-borne method can achieve the required coverage to monitor this change in time and space without prohibitive costs. Satellite observing technique will have to measure elevation and topography of sea ice directly in order to retrieve thickness. The ICESat mission, launched in 2002 (Zwally et al. 2002), provides height measurements using laser altimeter. With systematic observation of ice thickness, combined with ice area and ice drift measurements using satellite data, it will be possible to estimate global sea ice volume, fluxes and variabilities more accurately.

### 8.1.2 Sea Ice as a Barrier for Ship Traffic, Fisheries and Offshore Operations

The presence of sea ice represents a major limitation for ships and offshore operations at high latitudes in both hemispheres. The sea ice, which is on average 2–3 m thick, can only be penetrated by ice-strengthened vessels or icebreakers with a sufficient ice class. Most ships and fishing vessels are not ice-strengthened and must therefore avoid all ice areas. In many cases, when the ice concentration is 100% and the ice pressure is high, even the most powerful icebreakers have problems moving forward through the icepack. Offshore platforms for ice-covered areas must have much stronger construction than is required in ice-free waters. Harbors and loading terminals on the coast require stronger construction in areas of sea ice. In such areas, it is therefore of primary importance to monitor the sea ice daily and produce ice forecasts to assist ship traffic, fisheries and other marine operations. In the last 10 years, high-resolution Synthetic Aperture Radar (SAR) images from *RADARSAT-1* have been established as the main data source for ice monitoring in several countries (Bertioa et al. 2004). Canada, in particular, uses large amounts of wide-swath SAR images to monitor the Canadian ice regions. Figure 8-2 shows an example of an ice chart in the western Canadian Arctic produced by the Canadian Ice Service. In the Northern Sea Route, the longest ice navigation route in the world, Russia has built up an extensive ice service to support sea transportation and ice operations. Use of SAR data is not yet established as a regular service in the Northern Sea Route, but several demonstrations have been performed during dedicated icebreaker expeditions, as shown in Figure 8-3 (Pettersson et al. 1999; Johannessen et al. 2005). Several other countries are developing operational SAR ice-monitoring systems to support sea transportation, ice navigation and offshore operations in the ice-covered areas in the Northern Hemisphere.

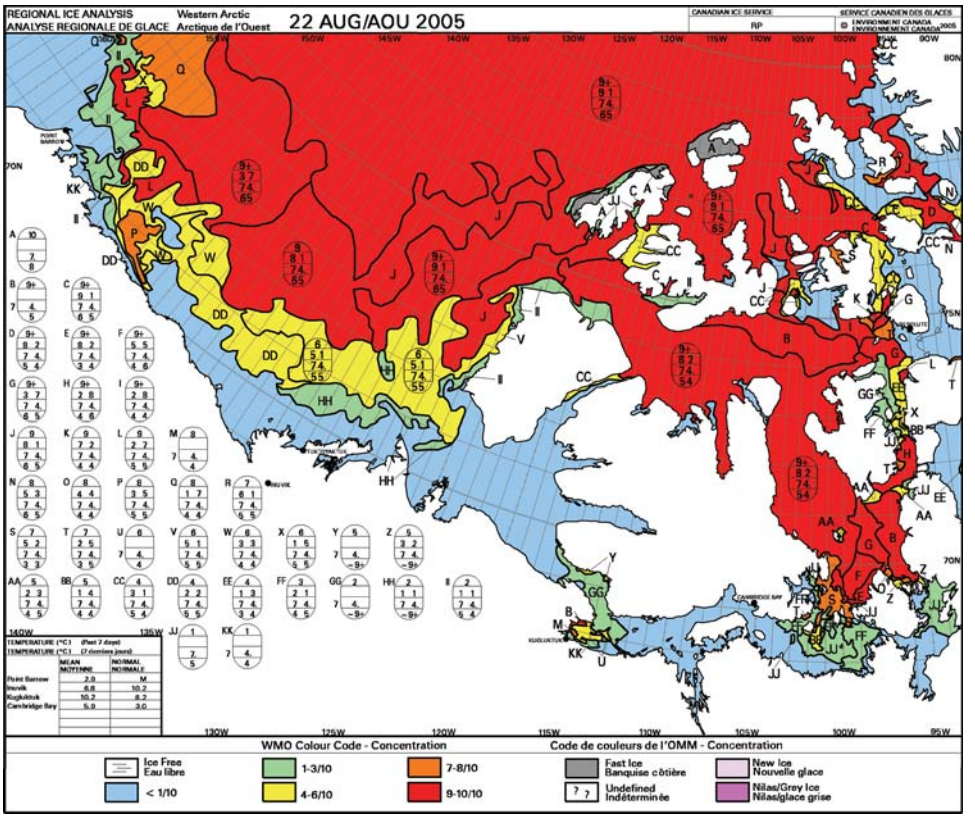


Figure 8-2 Example of weekly ice chart for the western Canadian Arctic produced by the Canadian Ice Service based on RADARSAT SAR images. Courtesy: Canadian Ice Service.

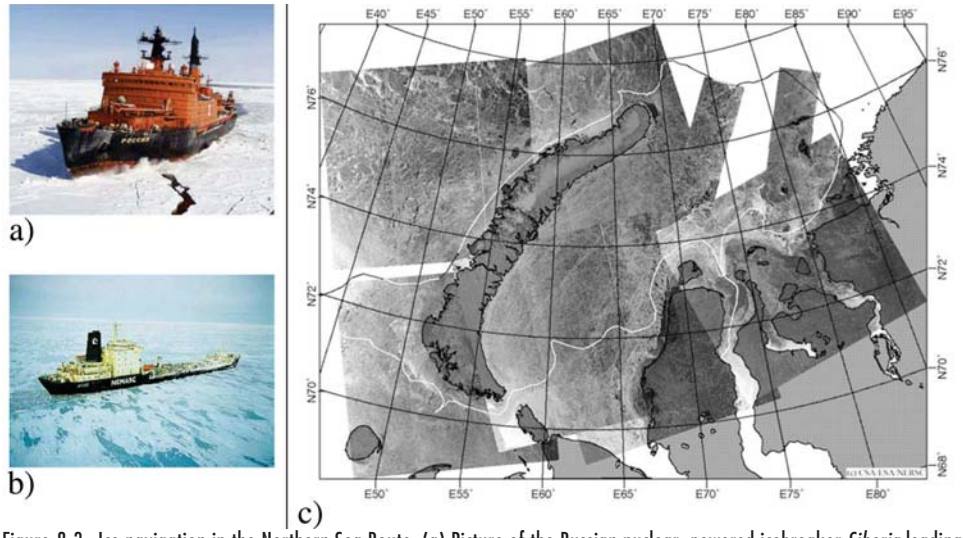


Figure 8-3 Ice navigation in the Northern Sea Route. (a) Picture of the Russian nuclear- powered icebreaker *Siberia* leading a convoy of cargo vessels sailing through 2-m thick first-year ice in the Northern Sea Route; (b) The Finnish icegoing tanker *Uikku* operating in sea ice; (c) SAR mosaic based on RADARSAT ScanSar and ERS-2 data obtained during the ARCDEV expedition in 1998. The line superimposed on the mosaic is the sailing route for the expedition from Murmansk to Ob Gulf. The two western–most images are described in more detail in Figure 8-20. Source: Pettersson et al. 1999. Courtesy: Murmansk Shipping Company, the ARCDEV Project, NERSC, The Canadian Space Agency & The European Space Agency.

## 8.2 BRIEF HISTORY OF SATELLITE SEA ICE MONITORING

Sea ice observation from coastal stations and ships has a history of more than 100 years. Regular sea ice charting, however, using aircraft and satellites has developed mostly since World War II. Aircraft survey was the main observation method until the 1980s, but use of satellite data has developed gradually over the last three decades and is now the most important observation method.

The first satellite sensors providing views of the large-scale structure and motion of sea ice utilized visible and infrared channels, such as those onboard the early *Nimbus*, *Tiros*, and *Earth Resources and Technology Satellite* (*ERTS*, later renamed *Landsat*). By the late 1960s, it was apparent that the sequential synoptic observations needed for sea ice and climate studies could not be acquired by visible sensors, which are limited to cloud-free and well-illuminated conditions. Sea ice exists in regions that are dark for several months and are frequently cloudy in the remaining months of the year (Gloersen et al. 1992).

Therefore, it has been necessary to develop observation methods using microwaves that are able to penetrate clouds and are not dependent on light conditions. The first passive microwave remote sensing systems for satellites were launched on the Russian *Cosmos 243* and *Cosmos 384* in 1968 and 1970, respectively. In the US, passive microwave technology was first used in remote sensing of sea ice during the late 1960s and early 1970s, when a prototype of the Electrically Scanning Microwave Radiometer (ESMR) was flown on *Nimbus-5* over the polar regions (Campbell 1973). The first atlas of Antarctic sea ice based on passive microwave data was produced by Zwally et al. (1983).

The period since 1970 has been one of great advancement in remote sensing of sea ice. After the ESMR period 1973–1976, a more advanced satellite instrument, the Scanning Multichannel Microwave Radiometer (SMMR) was operated on *Nimbus-7* for nine years, from 1978 to 1987. A similar instrument, the Special Sensor Microwave Imager (SSM/I) followed after the SMMR and has provided continuous measurements for more than 25 years. This series of similar spaceborne instruments provided the longest and first regular time series of global sea ice data, allowing studies of variability and trends of the ice area and extent in both hemispheres (Cavalieri et al. 1997; Johannessen et al. 1999). Passive microwave observations have fairly coarse resolution (typically 30 km) and are more suitable for large-scale or global monitoring than for regional and local observations. New passive microwave systems, such as AMSR-E, provide improved resolution of ice concentration charts, typically 6–10 km. Active microwave systems, such as real-aperture Side-Looking Radars (SLR) and Synthetic Aperture Radar (SAR), were developed during the 1970s and 1980s for aircraft surveillance and used in ice monitoring to provide detailed maps of the ice conditions, especially in areas of heavy ship traffic. Satellite SLR systems were used extensively in Russian ice monitoring during the 1980s and 1990s (Johannessen et al. 2000; Alexandrov et al. 2000).

Spaceborne SAR combines high spatial resolution with independence of cloud cover and light conditions, making it possible to observe sea ice with much better accuracy than visible and passive microwave methods. In 1978 *Seasat* was the first satellite that provided high-resolution SAR images of sea ice, but it only operated for about three months. The European Remote Sensing (ERS) program, which started in 1991, represented a major milestone in satellite SAR remote sensing of sea ice, because the two satellites *ERS-1* and *ERS-2* have operated continuously for more than 10 years and delivered tens of thousands of SAR images of ice-covered regions around the world. Since 1996 the Canadian *RADARSAT-1* has delivered wide-swath SAR images over large parts of the Northern Hemisphere sea ice. Arctic sea ice deformation fields and linear kinematics features have been derived from regular ScanSAR images and used to estimate ice area and volume production (i.e., Kwok

and Cunningham 2002). Since 2003 the European *ENVISAT* satellite has delivered wide-swath ASAR data, and ice observation is one of the main applications (Flett 2004; Sandven et al. 2004; Johannessen et al. 2005). Other microwave systems such as scatterometer and radar altimeter data have also shown promising results for observation of ice parameters.

## 8.3 PHYSICAL PROPERTIES OF SEA ICE

### 8.3.1 Large-scale Ice Parameters Defined by WMO

Sea ice terminology has been standardized by the Sea Ice Working Group of the World Meteorological Organization (WMO 2004), which established a nomenclature and the egg code for use in ice map production (Table 8-1 and Figure 8-4). The WMO nomenclature was defined for large-scale properties of sea ice and does not include the characteristics of ice structure on scales from cm to mm. Properties on this scale are important for the interaction of remote sensing signals with the ice-snow surface. Other limitations of the conventional ice codes from an ice navigation point of view are, according to Lensu et al (1996):

- The classification of ice types is unnecessarily detailed for younger and thinner ice types that exist only for shorter periods of time in the freeze-up and early-winter season. On the other hand, thicker, deformed and multiyear ice types are not characterized in the detail needed. The classification should be proportional to the decrease of ship speed and increase of damage probability.
- There is no quantitative reference to deformed ice types like rafted ice, in spite of the fact that deformed ice can be predominant and several times thicker than level ice.
- There is no quantitative reference to ice ridges, i.e., their size and frequency of occurrence.
- There is no reference to lead size, frequency or orientation.
- The relation of regional ice characteristics to what is experienced by an ice-going vessel is uncertain.
- The codes cannot optimally use the information that is available from SAR images.
- The terminology has no clear connection to geophysical ice models used in forecasting.

The main reason for these shortcomings is that the WMO nomenclature was defined in 1970, when no operative ice models existed, no high-resolution satellite data were available, and very little data on ice thickness, floe size and ridge distribution existed. The code clearly aims to display visual and mainly qualitative observations, for example those made onboard a vessel. It is not feasible that a single ice code would satisfy all possible requirements. With systematic use of SAR data and other new ice observation techniques, it is foreseen that new ice codes will be developed.

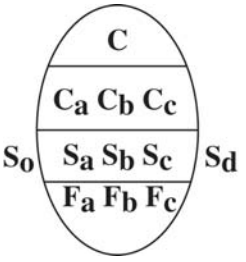


Figure 8-4 The World Meteorological Organization's Egg code for standard sea ice nomenclature defined in Table 8-1. Courtesy: The World Meteorological Organization

| | |
|---|---|
| $C_t$ | Total concentration of ice in area, reported in tenths. |
| $C_aC_bC_c$ | Partial concentration in tenths of thickest ($C_a$), second thickest ($C_b$) and third thickest ($C_c$) ice types with $C_a$, $C_b$ and $C_c$ 1/10 or more. If only one thickness type is present, it equals C and the second level is left blank. |
| $S_aS_bS_c$ | Stage of development (age) of ice concentration reported by $C_a$, $C_b$ and $C_c$. |
| $F_aF_bF_c$ | Predominant form of ice (floe size) corresponding to $S_a$, $S_b$ and $S_c$, respectively. |
| $S_oS_d$ | Development stage (age) of remaining ice types. $S_o$, if reported, is a trace of ice type thicker/older than $S_a$. $S_d$ is a thinner ice type that is reported when there are four or more ice thickness types. |

| $F_aF_bF_c$ | Form of ice | Width | $S_aS_bS_c$ | Stage of development | Thickness |
|---|---|---|---|---|---|
| 0 | Pancake | | 1 | New | < 10 cm |
| 1 | Brash | | 2 | Nilas | < 10 cm |
| 2 | Ice Cakes | < 20 m | 3 | Young | 10-30 cm |
| 3 | Small floe | 20-100 m | 4 | Gray | 10-15 cm |
| 4 | Medium floe | 100-500 m | 5 | Gray-white | 15-30 cm |
| 5 | Big floe | 500-2000 m | 6 | First year | > 30 cm |
| 6 | Vast floe | 2-10 km | 7 | Thin first-year/ White | 30-70 cm |
| 7 | Giant floe | > 10 km | 1. | Medium first-year | 70-120 cm |
| 8 | Fast ice | | 4. | Thick first-year | > 120 cm |
| 9 | Icebergs | | 7. | Old | |
| X | No Form | | 8. | Second year | no |
| C | Ice in strips in which concentration is C | | 9. | Multiyear | defined ranges |
| | | | | Icebergs | |

Table 8-1 Definition of the WMO Egg Code. Courtesy: The World Meteorological Organization

### 8.3.2 Small-scale Ice Structure and Growth of Ice

A complete description of ice freezing and melting, the main physical processes responsible for the large seasonal variability in sea ice extent and volume, should start with a discussion of the structure of the $H_2O$ molecule as it changes in the phase transition between solid and liquid. The fact that solid water has lower density than liquid water has the important implication that sea ice floats on top of the ocean. In this review, we will only

describe the most important physical properties very briefly, focusing on those which are important for remote sensing. The basic physical parameters of sea ice are temperature, salinity, crystal structure that incorporates brine and air, surface roughness, snow cover, and the presence of liquid water on top of the ice, which frequently occurs in summer when ice and snow melts at the ice surface.

Since sea ice is formed by the freezing of salt water, there are important effects of the salt during the freezing process; some salt is released from the ice as it is formed and is trapped in brine pockets of varying size. Ice formed during a winter season (first-year ice) contains typically from 6 to 10‰ salt if the ice is formed from normal sea water with salinity of 35‰. The brine gradually drains from the upper part of the ice, causing multiyear ice to have a very low salinity of less than 1‰ in the surface layer.

In the first stage of freezing, frazil ice is formed consisting of small ice crystals at the surface. As freezing continues and more ice crystals are formed, the crystals coagulate to form grease ice. Frazil ice and grease ice dampen the short gravity waves at the sea surface, which has significant impact on radar remote sensing of open ocean water. An example of this dampening is shown in the photograph in Figure 8-5a. If the freezing is allowed to continue without disturbance from surface waves, a weakly consolidated layer of elastic ice is formed. When this layer is less than 10-cm thick, it is defined as nilas. As it grows thicker and becomes less elastic, it forms gray ice (10–15 cm) and gray-white ice (15–30 cm). The process of brine drainage gradually replaces the brine pockets with voids of air that change the visual appearance from almost black nilas to bright gray and gray-white ice, which is significant in visual remote sensing of ice.

When wind and waves act on the ice-freezing process, which is the normal situation in the marginal ice zone, the grease ice forms pancakes—small rounded floes of elastic ice with a size of 30-cm to 3-m diameter. The wave action causes continuous collisions between the floes, generating raised rims typically 5–20-cm high (Figure 8-5b). The rims of the pancakes efficiently scatter the radar waves used in microwave remote sensing of sea ice.

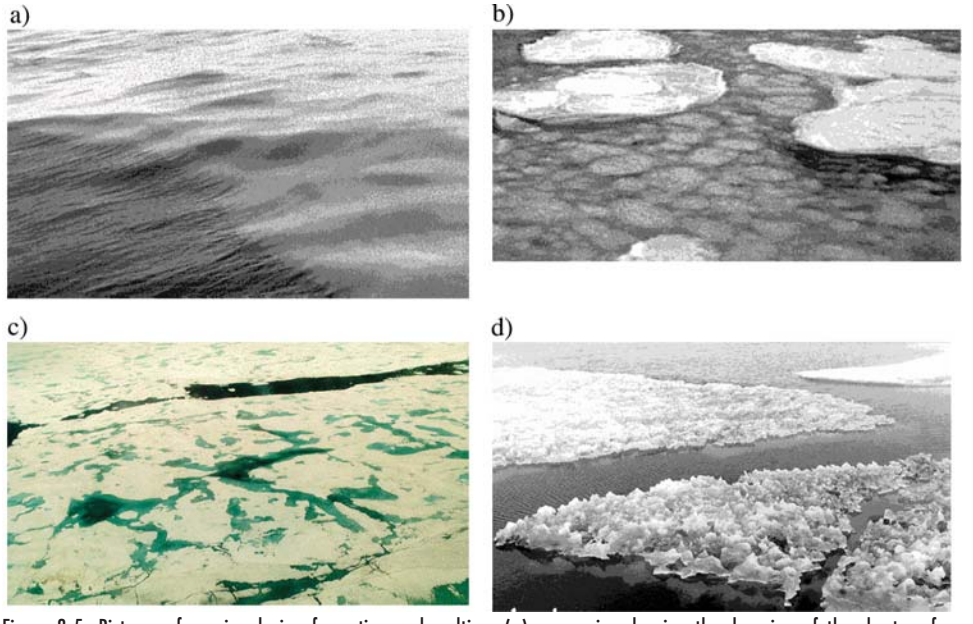


Figure 8-5 Pictures of sea ice during formation and melting; (a) grease ice showing the damping of the short surface waves; (b) pancake ice varying from 20–30 cm to 2 m in diameter; (c) melt ponds on top of the sea ice during the melt season (the distance across the picture is about 1 km); and (d) melting of ice and formation of melt ponds. Courtesy: NERSC.

In addition to the thermodynamic processes (freezing and melting) and the effects of the salt content, there is important mechanical forcing on the ice from winds and ocean currents that causes the ice cover to converge or diverge. Convergence causes ridges, rafted ice and underwater keels, while divergence generates leads and polynyas. The surface of leads and polynyas normally consists of open water or thin ice (nilas or gray ice), which is detectable by most remote sensing methods if the spatial resolution is good enough. The variability in surface roughness generated by ridging, rafting or other processes, such as pancake formation, is most appropriately observed by radar, since radar backscatter gives good contrast between rough and smooth ice surfaces.

In most areas, the sea ice is covered with layers of snow. This has an impact on remote sensing methods, especially visual methods for which snow cover determines the surface albedo. Snow is fairly transparent to microwave remote sensing wavelengths unless the snow is wet, or there are several layers of snow separated by thin ice. In regions with heavy snowfall, such as the East Greenland marginal ice zone, the ice can be loaded with wet heavy snow, which causes the whole ice floe to be flooded by sea water. This changes the microwave remote sensing signals from the ice. At the snow-ice interface, the snow is quickly re-crystallized, which also has an effect on the radar return signal.

The snow cover undergoes a characteristic seasonal cycle. In the winter season lasting from late autumn to the spring, defined by temperatures well below 0°C for both snow and ice, the snow cover is dry and practically transparent to microwaves. In late spring and early summer, when the temperature approaches 0°C, the snow becomes humid and eventually moist with melt pools at the interface between the snow and ice. Continued warming during the summer period, due to air temperatures above 0°C, can melt away much of the snow and the top layer of the ice. In periods of intense melting, a large part of the surface can be covered by melt pools (Figure 8-5c and d). For microwave remote sensing the amount of water at the surface is the most critical factor, while for optical remote sensing the variability of the surface albedo is most important. Typical values of the albedos are 0.8 for snow, 0.6 for dry ice and 0.2 for water-covered ice. The albedo is a key parameter controlling the incoming radiation, which determines the surface melt rate of snow and ice. The main factors that determine the microwave properties of new ice, first-year ice, multiyear ice and summer ice are illustrated in Figure 8-6.

At the beginning of the cold season, all ice that survived the summer season becomes multiyear ice. The top layer (first meter) of a multiyear floe is harder, has lower salinity and is more optically transparent than a first-year floe. The ridges of a multiyear floe are older and more rounded and smoothed compared to the ridges of a first-year floe. The smoothest areas are caused by refrozen pools covered with snow. The low salinity of the upper layer of multiyear ice makes it possible to discriminate first-year from multiyear ice by microwave remote sensing during winter. This discrimination is not possible in the melt season, due to the water and wet snow on top of the ice. Another phenomenon of importance for remote sensing during winter is the formation of frost-flowers in cold weather on top of thin, high-saline ice. These crystals, which have dimensions of a few cm, cause very high backscatter of the radar signal.

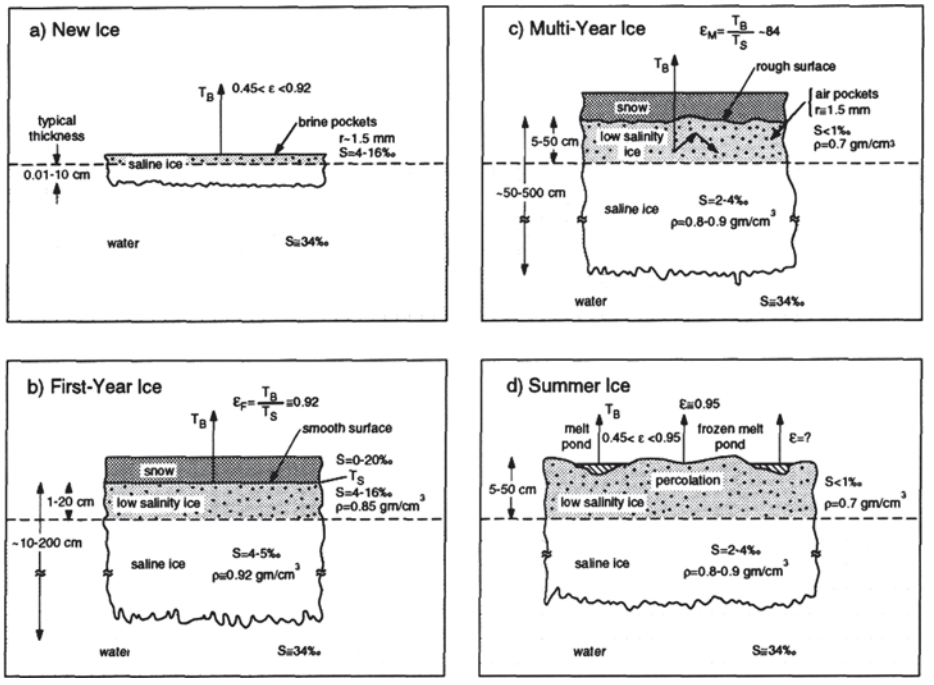


Figure 8-6 Four different sea ice types and the physical factors that have impact on the microwave properties that determine the brightness temperature. $T_B$: brightness temperature; S: salinity; $\varepsilon$: emissivity; $\rho$: density. Source: Zwally et al. 1983. Courtesy: NASA.

## 8.4 REMOTE SENSING PRINCIPLES AND ELECTROMAGNETIC PROPERTIES

### 8.4.1 Principal Methods, Instruments and Surface Characteristics

All remote sensing techniques for observing the Earth's surface use electromagnetic (EM) radiation in the visible/near-infrared (VNIR), thermal infrared (TIR) or microwave bands of the electromagnetic spectrum. There are three principal measurement techniques applicable to ocean and sea ice observations:

1. Measurement of the part of the incoming solar radiation that is reflected at the surface of the Earth (visual and near-infrared remote sensing)
2. Measurement of the thermal radiation from the surface (thermal infrared and passive microwave remote sensing)
3. Measurement of the return signal from an active source, such as a microwave radar, using several types of instruments that measure backscattered radiation from the surface

The sea ice surface can be considered to have three macroscopic components:

1. Open water in leads, polynyas and melt ponds on top of the ice in summer
2. Ice with varying amounts of salt water intrusions (salt pockets)
3. Snow on top of the ice

The following properties of the macroscopic components have impact on the remote sensing measurements:

1. Percentage and distribution of the three components
2. Temperature of the components
3. Salinity of the components and the distribution of salt intrusions in the ice
4. Crystal structure of the ice and the snow
5. Occurrence of snow and ice layers, and rough surfaces (e.g., floes, ridges, frost flowers).

In addition, there are variables defined by the remote sensing instrument that also have significant impact on the measurements:

1. Frequency (wavelength) of the radiation
2. Angle of incidence of the radiation
3. Polarization of the radiation if the view is not from directly above

The visible and infrared channels utilize intervals of the EM spectrum with high atmospheric transmission such as 0.4–2.5 μm, 3.5–4.0 μm and 10–13 μm. The EM waves in these intervals do not penetrate clouds, so observation of the Earth's surface requires cloud-free conditions. This is a rather severe limitation, because sea ice occurs in regions where clouds are present most of the time. Microwaves, at wavelengths longer than 0.3 cm, generally penetrate cloud, making it feasible to obtain regular, daily observations.

The most common satellite instrument for measuring VNIR and TIR is the Advanced Very High Resolution Radiometer (AVHRR), which provides images with resolution of about 1 km in typically five different frequency channels. The basic parameter observed by VNIR is the albedo, or reflection coefficient. The albedo is measured as a value between 0 (total absorption of the sunlight) and 1 (total diffuse reflection of the sunlight). Snow covering most of the sea ice surface gives albedos ranging from 0.8 for new snow to 0.6 or lower as the snow gets older. For very old and wet surfaces of ice and snow, the value can be as low as 0.2. Open water has an even lower albedo, varying somewhat with incidence angles and wind. The vertical reflection coefficient of calm pure water is only about 0.02. For snow and ice, the visual albedo decreases slowly with increasing wavelength. In the near-infrared, the decrease is more rapid for most snow and ice types, reaching very low values below 0.1 for wavelengths over 1.5–2.0 μm. This can be used to discriminate snow and ice from clouds. Snow and clouds often show a similar signal in the visual part of the spectrum, which can be a major problem.

For TIR the measured parameter is emitted energy, which is a function of surface temperature and emissivity. The emitted energy, expressed as the radiance received by the radiometer, is used as input to the Planck equation of radiation to find the surface temperature $T_s$, assuming that the emissivity $\varepsilon$ of the surface is known. For water, the value of $\varepsilon$ in the most-used thermal spectral band of 10–12 μm is very high and stable, about 0.99, and accurate measurements (to 0.1–0.2°K) of the water surface skin temperature can be made. Snow and ice also have high emissivity in this region but with more variation, and approximate temperature measurements of the surface (to 1–2°K) can be made.

Passive microwave radiometers measure the emitted microwave radiation in several channels and polarizations. The measured parameter is brightness temperature $T_b$, which is defined by the relation $T_b = T_s * \varepsilon$, where $T_s$ is the real surface temperature and $\varepsilon$ the emissivity. For the most often used frequencies between about 6 and 90 GHz, the emissivity of both ice and water show large variations. While $e$ for calm water can be calculated quite accurately from the electric properties, the value and variation of $\varepsilon$ for the various forms of ice and snow is less accurately known, and therefore often has to be empirically measured. Passive microwave footprints are large, typically 10–60 km depending on frequency, im-

plying that many different components of snow/ice/water can be present in one measurement. Multi-frequency measurements are widely applied in algorithms for determining the relative coverage (concentration) of sea ice, to be further discussed in Section 8.5.

Active microwave observations can be obtained by several types of instruments. The most common are Synthetic Aperture Radars (SAR), Side-Looking Radars (SLR) and scatterometers. The SAR instruments provide high-resolution images, with pixel size down to about 10 m, while the SLR provides medium-resolution images with resolution of 1–2 km. Scatterometer data have coarser resolution, varying from 10 km to about 50 km. For active systems, the most important parameter is the backscatter coefficient, called sigma-nought ($\sigma_0$), which expresses a measure of the energy backscattered towards the source of the radiation, at a scattering angle of 180°. The backscatter coefficient and other related parameters are further discussed in Section 8.6.

### 8.4.2 Electromagnetic Properties of Ice, Snow and Water Surfaces

The most important electromagnetic properties of any surface are *reflection* and *emission*. The latter, expressed by a dimensionless coefficient called *emissivity*, can be computed from the complex dielectric constant (or the relative permittivity) $e = e' - i\,e''$, which characterizes the electrical properties of the medium. $e'$ is referred to as the dielectric constant and $e''$ as the dielectric loss factor. Alternatively, $e$ can be estimated from the complex index of refraction, $n$ where $n^2 = e$. The reflection coefficient $r$ is defined as

$$r = |(n-1)/(n+1)|^2 \tag{8-1}$$

The dielectric constant, together with the surface roughness of the target, determines the emissivity. The seasonal dependence of sea ice emissivity for typical first-year and multiyear ice is illustrated in Figure 8-7.

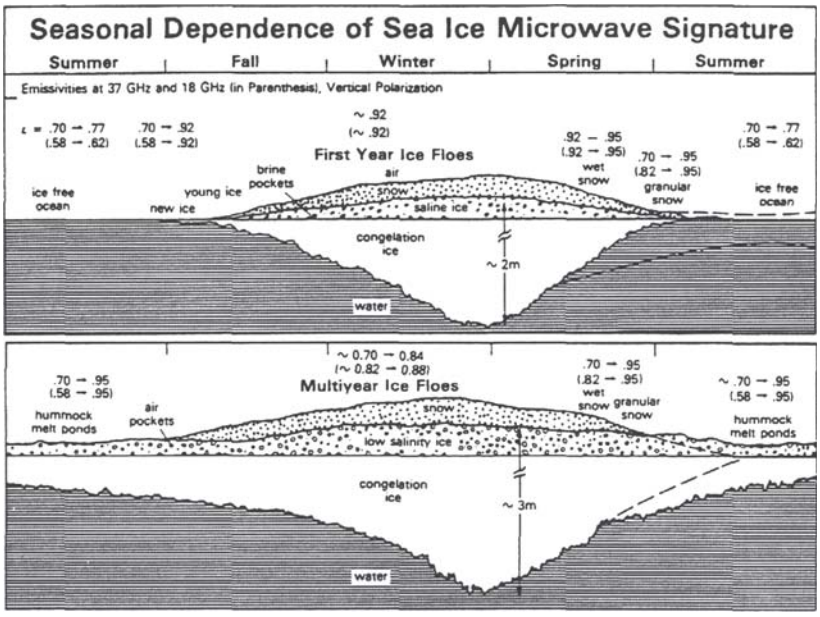


Figure 8-7 Seasonal dependence of sea ice emissivity in the Arctic for 18 and 37 GHz, the most important frequencies used to estimate ice concentration. Source: Comiso 1983.

#### 8.4.2.1 OPEN WATER

Observation of open water is necessary as a reference for identification of sea ice, especially for detection of the ice edge and areas of new ice formation. Within sea ice, open water can occur in leads and polynyas, or in melt ponds on top of the ice in summer. Examples of reflection coefficients for calm, pure water at two different wavelengths and normal incidence angle using Equation 8-1 are:

- For visual radiation at 0.55 µm, $n$ is 1.33, which gives $r = 0.02$
- For infrared radiation at 11 µm, $n$ is 1.20, which gives $r = 0.008$

The low reflection coefficients show that water is dark in the visible wavelengths and almost a black body at infrared wavelengths. For microwave remote sensing, water temperature and salinity are also important. Formulae for computing reflection/emission coefficients from the dielectric constant can be found in Strogyn (1971). Examples of reflection and emission coefficients, at normal incidence, 273K, and 35% salinity are:

- For microwave radiation at 10 GHz, $e = 38 - 41i$, $r = 0.61$ and $? = 0.39$
- For microwave radiation at 37 GHz, $e = 9 - 18i$, $r = 0.47$ and $? = 0.53$

Sea water is therefore a gray body at microwave frequencies, with emissivity varying strongly with frequency.

#### 8.4.2.2 MICROWAVE ELECTRICAL PROPERTIES OF ICE

In the microwave wavelength region and for the physical temperatures encountered, the Rayleigh-Jeans approximation to the Planck radiation law holds. The radiated power, usually expressed as brightness temperature $T_b$, is therefore proportional to the physical temperature $T_s$ at the surface. Most real objects emit only a fraction of the radiation that a perfect emitter would at the same physical temperature. This fraction defines the emissivity of the object as $T_b / T_s$. Spatial variations in microwave $T_b$ observed over the surface of the Earth are due primarily to variations in the emissivity of the surface material and secondarily to variations in temperature.

The value of the dielectric constant $e'$ for freshwater ice has been measured as 3.17 at 10 GHz and varies little with frequency (Hallikainen and Winebrenner 1992). For saline first-year ice, $e'$ is higher and strongly dependent on both temperature and salinity of the ice. Only a small amount of brine will alter the dielectric constant of the ice, due to the great value of $e$ for salt water. A brine volume of 4% was found to give apparent dielectric constant of about 4.5. Lower temperature will reduce the dielectric constant.

For sea ice, the dielectric constant $e'$ is relatively constant with frequency above 1 MHz, but $e''$ is not. There is a minimum in $e''$ at 3–8 GHz with higher values at lower and higher frequencies. For first-year ice at 10°C and 8‰ salinity, the minimum $e''$ is approximately 0.3. As temperature decreases, $e''$ increases as precipitated salt goes back into solution; $e''$ increases with salt content. Multiyear ice has a lower $e''$ than first-year ice and its temperature dependence is weaker. Thus, microwave radiation penetrates deeper into multiyear than first-year ice.

Empirical relations have been established for the dielectric constant and hence emissivity for sea ice at different microwave frequencies (Figure 8-8). For example, the emissivity of sea water at 19 Ghz is about 0.44 compared to 0.92 for first-year ice and 0.84 for multiyear ice. In contrast to water, it is not only the temperature, salinity, incidence angle and polarization that determine the emissivity. The structure of the crystals and of the brine pockets, different for various ice types and ice ages, are also important.

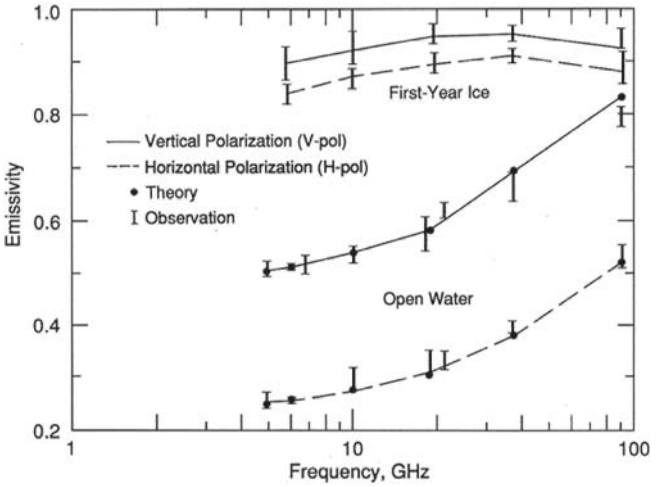


Figure 8-8 Theoretical and observed emissivities for first-year ice and calm water, for both vertical and horizontal polarization as a function of frequency. Source: Carsey 1992.

#### 8.4.2.3 MICROWAVE ELECTRICAL PROPERTIES OF SNOW

There is a large difference in electrical properties between dry snow and wet snow with high liquid water fraction. Snow without salt can be considered dry in temperatures below -1°C. Wet snow has high $e''$ with corresponding high absorption and emission. In summer, therefore, microwaves will only sense the top layer of the snow cover on the ice.

In winter, dry snow is almost transparent with very small $e''$. However, the bottom snow layer on first-year ice can contain salt, and with 4‰ salt the effect is to double the value of $e''$ from the value of 0.3 for pure ice. The dielectric constant $e'$, which is independent of frequency, is only weakly dependent on temperature, and increases with the snow density. For a density 0.2 g/cm$^3$, $e'$ has a value of approximately 1.3.

## 8.5 PASSIVE MICROWAVE METHODS AND APPLICATIONS

### 8.5.1 Retrieval of Ice Concentration

The radiative transfer equation is the basis for the development of algorithms that convert the satellite radiance data into geophysical parameters. The microwave radiances received by the satellite are composed of various contributions from the Earth, atmosphere and space (Figure 8-9). The radiation received by the satellite, which is a function of wavelength and polarization, can be expressed by an equation consisting of four terms:

$$T_b = \underset{(1)}{\varepsilon T_s e^{-\tau}} + \underset{(2)}{T_{up}} + \underset{(3)}{(1-\varepsilon) T_{down} e^{-\tau}} + \underset{(4)}{(1-\varepsilon) T_{sp} e^{-2\tau}} \qquad (8\text{-}2)$$

where $T_b$ is brightness temperature observed by the satellite. Term *(1)* is the part of the signal that comes from the surface of the Earth, where $T_s$ is real surface temperature, $\varepsilon$ is emissivity, and $e^{-\tau}$ represents atmospheric absorption. Term *(2)* $T_{up}$ is the atmospheric upwelling radiation, in term *(3)* $T_{down}$ is the atmospheric down-welling component, and in term *(4)* $T_{sp}$ is the cosmic background component (Swift and Cavalieri 1985).

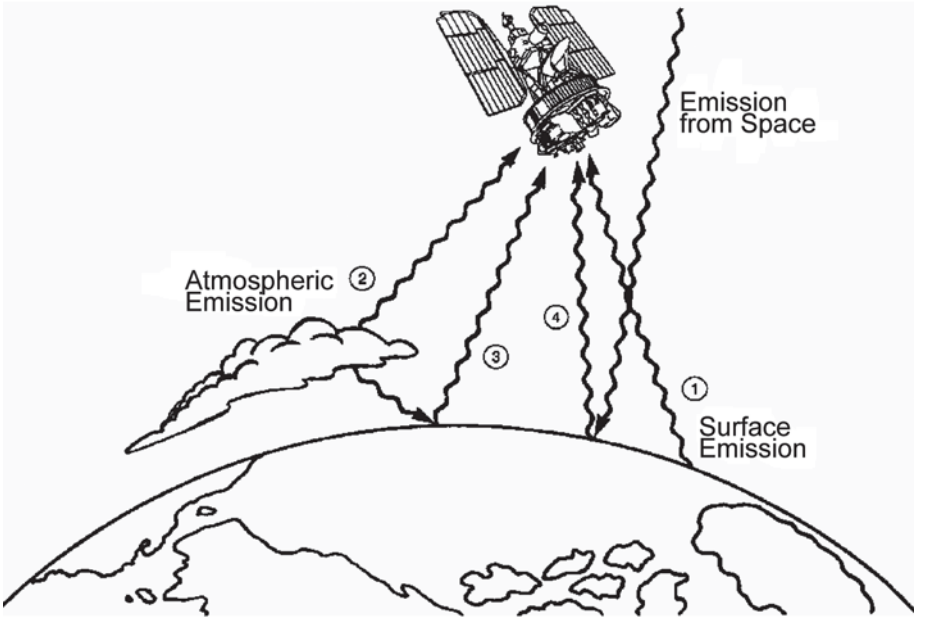


Figure 8-9 The main components of the brightness temperatures, observed by passive microwave radiometer in a satellite, are expressed by four terms in the radiative transfer equation. Source: Swift and Cavalieri 1985.

There are several algorithms for estimation of sea ice concentration from brightness temperature observed in several channels and both polarizations (Steffen et al. 1992). An example is NORSEX-85H, which is an extension of the NORSEX algorithm developed by Svendsen et al. (1983) based on the SMMR data available from 1978 to 1987. The 85H version takes advantage of the improved spatial resolution of the 85 GHz channels provided by the SSMI system now in operation (Svendsen et al. 1987). The NASA Team algorithm, developed by Cavalieri et al. (1984, 1991), has been widely used and runs operationally to produce daily ice concentration maps. Other algorithms include the Bootstrap algorithm by Comiso (1995) and Comiso et al. (1997), the AES York algorithm (Rubinstein et al. 1994), and more recently the SEALION algorithm for Antarctica (Kern 2001) and the ARTIST algorithm (Kaleschke et al. 2001). The two latter algorithms address particularly the effects of weather on the 85-Ghz channel. The algorithms use different combinations of sensor channels, polarizations and tie points. The main outputs are concentration of total ice cover, first-year fraction and multiyear fraction. The first algorithms developed in the 1980s have undergone various degrees of validation over many years (Steffen et al. 1992), and are generally robust for retrieving total ice concentration. The accuracy is on the order of 5% during winter conditions, increasing to more than 10% in the melt season, assuming a sampling scale of about 30 km. Retrieval of fractions of multiyear and thin ice types has been proposed, but with less accuracy. Newer algorithms have focused on use of the 85-Ghz channel for higher resolution of the concentration (typical sampling scale of 12 km) and improved correction of weather effects that impact this channel. Examples of applications are presented in the next section.

### 8.5.2 Global and Regional Ice Area Analysis of Merged SMMR and SSM/I Data

The brightness temperature data from the SMMR (1978–1987) and the SSM/I (1987 to present) have been used to establish merged time series for calculation of total ice concen-

tration from which total ice area and total ice extent (the area of ice-affected ocean within the ice/open water boundary) are derived. Examples of total ice concentration maps for the Arctic and Antarctic are shown in Figure 8-1. The merged SMMR and SSMI data have shown a decreasing trend in Arctic ice area and extent to be about $-0.3 \times 10^6$ km$^2$ per decade (Bjørgo et al. 1997; Johannessen et al. 1999), corresponding to ~3% per decade (Figure 8-10a, b), with no significant change in the Antarctic. The 3% per decade decrease in the Arctic ice extent was subsequently corroborated in a separate analysis (Cavalieri et al. 1997). The capability to monitor interannual variations in multiyear ice area from SMMR and SSM/I data has recently been exploited using winter data, when first-year and multiyear ice signatures permit their distinction (Johannessen et al. 1999). The analysis revealed a relatively large (~7% per decade) reduction in the multiyear ice area 1978–1998 (Figure 8-10c), compared with a ~2% per decade decrease in the total ice area in winter. Regional analysis of ice areas and extent shows that the largest reduction in ice extent between 1978 and 1996 is found in the Barents and Kara Seas where the extent has decreased by about 10% per decade (Parkinson et al. 1999). The time series of passive microwave data has also been used to determine the onset of spring melt and autumn freeze-up of Arctic sea ice. From 1979 to 1996 the number of melt days per year has increased by 0.5 days per year for the whole Arctic sea ice area with a standard deviation of $\pm$ 10 days (Smith 1998). The reduction of the Arctic sea ice cover observed in passive microwave data is also supported by observational evidence of thinning of the sea ice cover (Rothrock et al. 1999) and by model simulations (Johannessen et al. 2004).

## 8.6 IMAGING RADAR PRINCIPLES

### 8.6.1 Basic Properties of Imaging Radars

Imaging radars provide their own source of illumination in the microwave portion of the EM spectrum, at wavelengths about 10,000 times longer than those in the visible part of the spectrum. This allows radars to operate independently of solar illumination and to penetrate clouds and precipitation. An imaging radar sends out microwave energy that strikes an object and is partially reflected back. The radar system senses the intensity of the reflected wave and at the same time measures the time taken for a round trip. Radar systems differ from visible and infrared systems in that radar:

- Detects electrical properties of the surface rather than visible color or thermal temperature
- Senses the surface roughness of the area being imaged
- Produces images with speckle due to the coherent nature of the system
- Produces images with certain geometrical distortions, such as slant range geometry, image layover and shadowing
- Records the phase and polarization characteristics of the reflected microwave pulse
- Senses motion of objects in the imaged area

The next section gives a brief overview of the remote sensing parameters used in observation of sea ice by spaceborne radar. Extensive descriptions of radar remote sensing principles have been published by Ulaby et al. (1982a, b) and more specific radar remote sensing methods for sea ice have been described in the books edited by Carsey et al. (1992), Haykin et al. (1994), Tsatsoulis and Kwok (1998) and Jackson and Apel (2004).

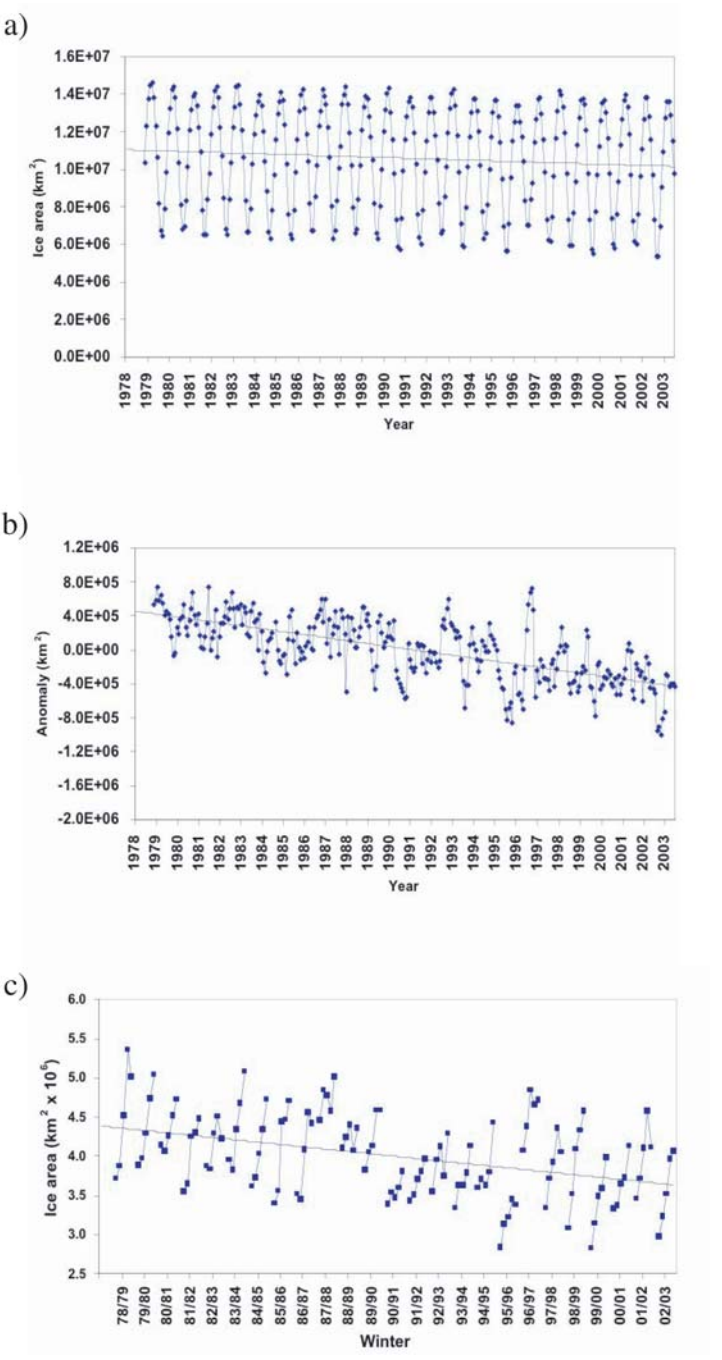


Figure 8-10 Time series of Arctic ice area derived from merged SMMR and SSM/I satellite passive microwave data: (a) monthly mean and (b) anomalies in ice area (departure from mean annual cycle) in 1978–2003 where the linear regression indicates a ~31,000 $km^2$ $yr^{-1}$ decrease, corresponding to ~3% per decade, and (c) fraction of multiyear (i.e., having survived the summer melt) sea ice area in winter (November–March), 1978–2003, where the linear regression indicates a ~30,000 $km^2$ $yr^{-1}$ decrease, corresponding to ~7% per decade. Source: Johannessen et al. 1999. Courtesy: NERSC.

### 8.6.2 Some Important Parameters and Properties of Imaging Radars

The imaging geometry of present spaceborne SAR systems is shown in Figure 8-11. Most SAR systems look to the right of the orbit, away from *nadir*, which is the ground projection of the satellite orbit. The two main orientations on the ground are *azimuth direction* (along the satellite orbit) and *range direction* (the look-direction of the SAR, cross-track, perpendicular to the orbit). A SAR measures the travel time of the reflected microwaves and converts this to a measurement of *range* to the target, defined as

$$R = c\tau/2 \tag{8-3}$$

where *c* is the speed of light and *?* is the two-way travel time of the radar pulse. In imaging theory, *resolution* of a radar system is defined as the distance two objects must be separated to be detected as two unique targets. Two different principles determine the resolution of a radar system. First, the along track, or azimuth resolution $r_a$ is defined by the beamwidth *?* of the radar, which is the angle by which the radar beam expands and is a function of the antenna size

$$r_a = R\beta \tag{8-4}$$

Second, the beamwidth of the radar is a function of the antenna length, with a larger antenna producing a narrower beam. For real aperture radar, such as Side-Looking Radars, the only way to obtain fine azimuth resolution is to have a very short range or a very large antenna. Synthetic Aperture Radar (SAR) overcomes this problem by utilizing the along-track motion of the satellite (or aircraft) to produce a very large, "synthetic" antenna.

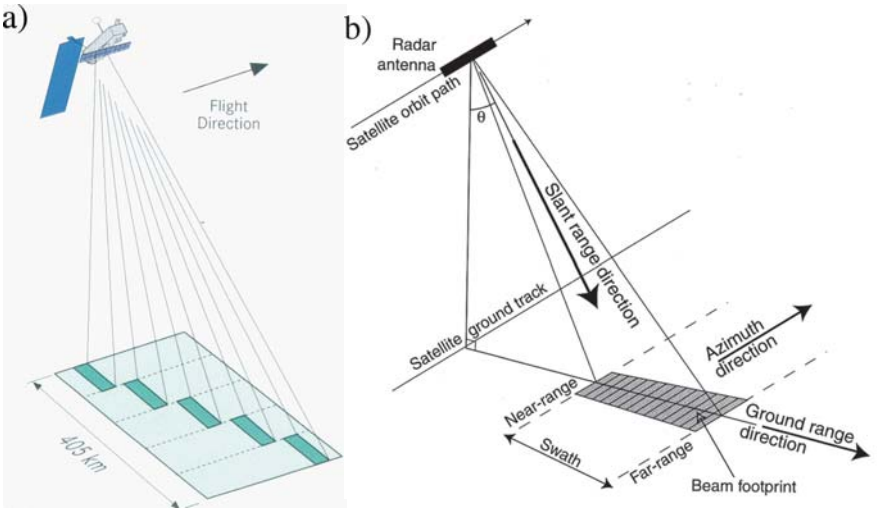


Figure 8-11 (a) Illustration of ENVISAT ASAR geometry for the Wide-swath Mode, which consists of five narrow-swath beams, each covering a width between 70 and 100 km. Source: ESA 2002. The width of the wide-swath image is about 400 km. (b) Illustration and main terms of satellite SAR geometry. Source: Robinson 2004. Courtesy: Springer, Praxis Publishing Ltd.

The range resolution $r_r$ of a radar system is defined by the transmitted radar pulse

$$r_r = ct_p/2 \tag{8-5}$$

where $t_p$ is the duration of the transmitted radar pulse and c is speed of light.

Imaging radars operate in the microwave frequencies between 400 MHz and 35.2 Ghz, corresponding to wavelengths between 62 and 0.85 cm. Radar frequencies are identified by letter designations. The most commonly used are K-band (30 GHz, 1 cm), X-band (9.4 GHz, 3.2 cm), C-band (5.3 GHz, 5.7 cm), L-band (1.25 GHz, 23.5 cm) and P-band (450 MHz, 62 cm). At these wavelengths the EM-waves are not appreciably attenuated by clouds, precipitation or the Earth's atmosphere. Therefore, good quality radar images can be obtained in all kinds of weather and light conditions. Another characteristic of imaging radar systems is polarization, which is defined as the direction of the electric vector of the transmitted or received EM wave. Visible light is unpolarized because the direction of the electric vector is randomly distributed. For radar systems it is common to emit pulses that are either horizontally (H) or vertically (V) polarized. The radar antenna can receive either the horizontally or vertically oriented return signal, or both.

In contrast to visible and infrared remote sensing, radar remote sensing is extremely sensitive to the surface roughness. For smooth surfaces, there is specular reflection of the radar waves, and for off-nadir viewing, no energy is reflected back to the radar. As the surface becomes rougher, the radar wavelengths interact with the surface in a way that causes diffuse reflection (Figure 8-12). The amount of roughness controls the distribution of the reflected energy, and thus the intensity in the radar image. For a microwave radar, a surface is rough if

$$\Delta h \cos q_1 > \lambda/8 \tag{8-6}$$

where $\Delta h$ is the vertical scale of the surface roughness, $q_1$ is the incidence angle and $\lambda$ is wavelength.

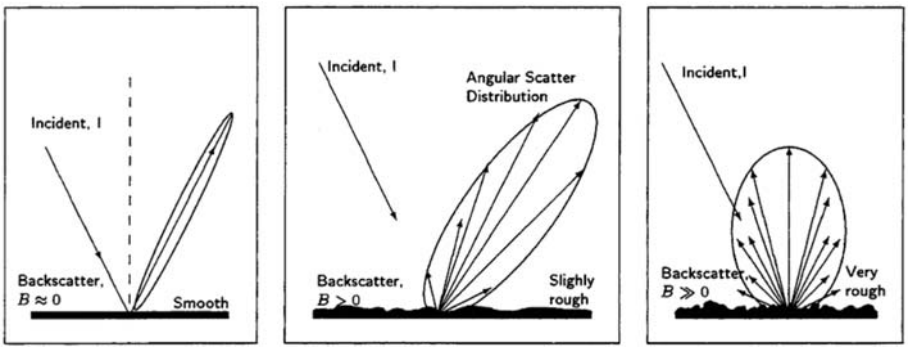


Figure 8-12 Qualitative illustration of the effect of varying surface roughness on the reflection and spreading of microwaves in X- and L-band. Source: Onstott and Shuchman 2004. Courtesy: NOAA.

### 8.6.3 The Radar Equation

All radar measurements can be described by a basic equation that relates power, distance, reflectivity and antenna characteristics. The equation can be formulated as

$$P_R = \frac{P_t G \sigma A}{(4\pi)^2 R^4} \tag{8-7}$$

where $P_R$ is power received, $P_t$ is power transmitted, $G$ is the gain of the antenna, $\sigma$ is the radar cross section, and $A$ is antenna area. $A$ can also be expressed as $\lambda^2 G/4\pi$. Equation 8-7 is a product of four terms

$$P_R = \frac{P_t}{4\pi R^2} G \frac{\sigma}{4\pi R^2} A \qquad (8\text{-}8)$$

(1) (2) (3) (4)

The energy of the outward-propagating wave, which is spherically expanding, is given by term *(1)*. This spherically expanding wave is focused down to an angular beamwidth by the antenna so that the fluxes become higher by a factor G, term *(2)*. The focused energy impinges on an object that has a radar cross section $\sigma$, which is defined as the equivalent of a perfectly reflecting object of a given area that reflects isotropically (spherically) as shown by term *(3)*. Finally, the antenna area, *A*, term *(4)*, intercepts the portion of the reflected wave received.

The basic radar return equation is general and can be applied to an object of any shape or composition. For imaging over distributed areas of terrain or ocean, a reflection coefficient, $\sigma_0$, is defined as the radar cross section, $\sigma$, per unit area. The radar equation (Equation 8-7) can then be expressed as

$$P_R = \frac{\lambda^2}{(4\pi)^3} \int \frac{P_t G^2 \sigma_0}{R^4} dA \qquad (8\text{-}9)$$

The radar-scattering coefficient, $\sigma_0$, also called backscatter coefficient, is important because it is an absolute measure of scattering behavior. It is a function of frequency, incidence angle, polarization, and the scattering characteristics of the illuminated area. It is defined to be unity for a surface of small metal balls, which exhibit ideal diffuse scattering (no variation with incidence angle). The backscatter from various sea ice surfaces is generally much smaller than unity at the most-used incidence angles (20°–50°). Examples of measurements of $\sigma_0$ by SAR for different ice types and surface conditions are discussed in Section 8.7.

## 8.7 ACTIVE MICROWAVE OBSERVATIONS OF SEA ICE

The most important active microwave remote sensing instrument for ice monitoring is the Synthetic Aperture Radar (SAR), which provides high-resolution images of the Earth's surface. The development of airborne-SAR observing systems during the 1970s and 1980s paved the way for the satellite SAR systems *Seasat*, *ALMAZ-1*, *JERS-1*, *ERS-1* and *-2*, *RADARSAT-1* and *ENVISAT*. *ERS-1* and *-2* and *RADARSAT-1* have been operational for many years and have provided large amounts of SAR images for sea ice observation, in particular the RADARSAT ScanSAR data. In 2003 *ENVISAT* started to provide multimode SAR data. Other active microwave methods used for ice observations include scatterometers, radar altimeters and real aperture radars (Side-Looking Radars - SLR) on Russian satellites.

### 8.7.1 Interaction Between Active Microwaves and Sea Ice Characteristics

The radar backscatter from sea ice is highly dependent on physical ice properties such as salinity, temperature, surface roughness, snow layers and presence of water. Multiyear ice is characterized by low salinity in the surface layer (< 2.0‰), which allows penetration of the microwaves into the ice (volume scattering). First-year ice, on the other hand, has higher

salinity in the surface layer (5–7‰), which causes mainly surface scattering. The volume scattering from the multiyear ice tends to give higher backscatter than the surface scattering from smooth first-year ice. However, first-year ice can also give higher backscatter due to rough surface caused by ridges, small floes with many irregular edges and snow crystals. Open ocean gives very low backscatter in the case of no wind. Usually some wind is present, causing short surface waves and high backscatter values (Shuchman and Onstott 1990). The various stages in ice formation and ice growth during the winter season generate variable backscatter, which can be difficult to interpret. A number of field experiments have been conducted since the ERS program started in 1991, with the purpose of studying SAR backscatter for various ice types and conditions. As an example of a SAR sea ice experiment, we present in the next section some results of the Seasonal Ice Zone Experiment (SIZEX 92), which was the first ERS-1 SAR ice winter validation experiment in the Barents Sea (Sandven et al. 1999). After the launch of *RADARSAT-1* in 1995, extensive efforts have been made to develop sea ice observation and analysis systems, in particular the RADARSAT Geophysical Processor System (RGPS). A brief review of results from the RGPS system is described in Section 8.7.3. The RGPS system and other recent advances in analysis of SAR data for the polar oceans are described in more detail in Tsatsoulis and Kwok (1998), Jackson and Apel (2004) and Johannessen et al. (2005).

### 8.7.2 Analysis of ERS-1 SAR Images in the Seasonal Ice Zone Experiment (SIZEX 92)

During SIZEX92, C-band ERS-1 SAR images with VV-polarization were downlinked and processed at Tromsø Satellite Station and distributed to the Nansen Environmental and Remote Sensing Centre in Bergen for real-time use during the field experiment and for further analysis. SAR backscatter values from several ice types and open water conditions were analyzed. Each image was averaged from 16 × 20-m pixels to 100 × 100-m pixels, thereby removing much of the speckle noise. The images were then normalized to an incidence angle of 23° (in the center of the swath) by applying antenna pattern and incidence angle/distance corrections as described by ESA (Caneva 1992). Finally, the pixels in the images were calibrated to $\sigma_0$ backscatter values by the relation $\sigma_0 = 20 \log V - 46.9$, where $V$ is the digital value of the 8-bit images. The lowest backscatter observed in the images had values of $V = 14$ (grease ice), and this was assumed to correspond to the noise floor of -24 dB. The accuracy of this calibration is estimated to be 1–2 dB. Increasing digital values correspond to higher backscatter, with values increasing to about +1 db for V = 255 (Figure 8-13).

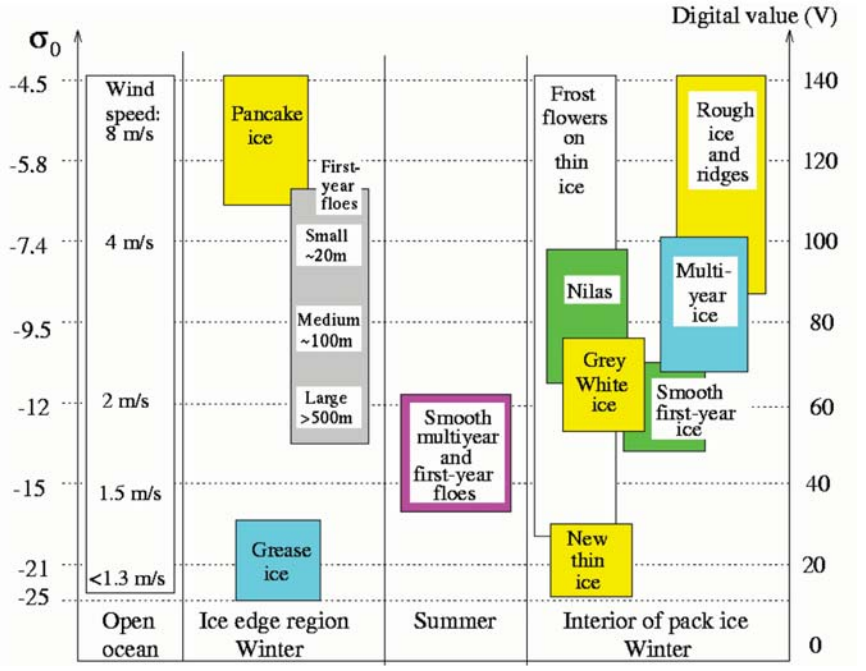


Figure 8-13 Backscatter coefficient for ERS SAR (C-band, VV-polarization and 23° incidence angle), expressed in $\sigma_0$ (left) and digital value (right), for different regions and ice types as observed during the SIZEX92 experiment and other SAR ice validation experiments. Note that ERS SAR backscatter for different wind speeds over open ocean are included for comparison because the SAR backscatter for open water can often be similar to some of the ice types. Source: Sandven et al. 1999.

The primary *in situ* measurements were profiles of snow and ice parameters taken at several sites from ships and helicopters. At each site several ice cores were drilled to obtain some spatial statistics of the ice parameters. The ice cores were analyzed for temperature, salinity, density and brine volume. Ice type was identified, ice thickness was measured and surface roughness was characterized. Snow thickness, temperature, grain type, grain size, density and layer description were also obtained at each site. An example of a SAR scene extending from open water to the interior of the ice pack is shown in Figure 8-14a. From the SAR images and the *in situ* observations, the ice conditions in this part of the Barents Sea could be divided into three zones, reflecting different physical processes. In the following discussion each of these zones, which are denoted A, B and C, are described in terms of their SAR signatures. Results of classification of the SAR images into six classes according to Sandven et al. (1999) are shown in Figure 8-14b.

### 8.7.2.1 ZONE A: THE INTERIOR OF THE ICE PACK

In the upper left part of the SAR image in Figure 8-14a, many multiyear floes were found about 100 km into the ice pack. The backscatter value of these floes was typically -9.0 $\pm$ 1.5 dB. Between the multiyear floes, areas of undeformed first-year ice, typically 2–3 m thick, were observed. This ice had backscatter values from -10 to -13 dB. Refrozen leads with smooth thin ice had the lowest backscatter values, between -19 and -13 dB. Ridges and leads with open water were found to have variable and higher backscatter, above -8 dB. In the interior of the icepack, the ERS-1 SAR demonstrated good capability to discriminate between: a) young ice in refrozen leads, b) multiyear ice in large floes, c) rubble fields/ridges, and d) smooth first-year ice using simple thresholding of backscatter values. The Wackerman classification method can separate multiyear, undeformed first-year, and to some extent deformed first-year and young ice in the leads.

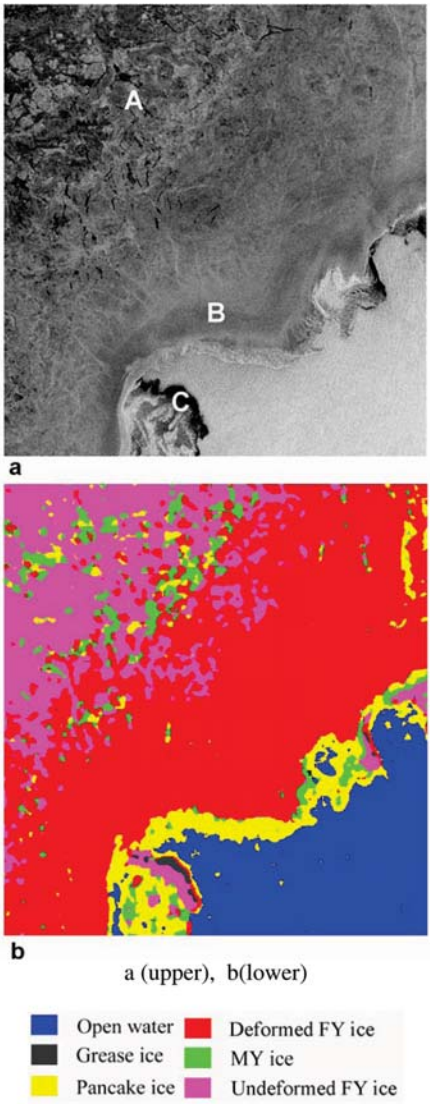


Figure 8-14 (a) Example of ERS-1 SAR image from the SIZEX experiment, covering 100 by 100 km of the marginal ice zone with characteristic zones denoted as A, B and C; (b) The result of a classification of ice types and open water from the SAR image above. The color code for the classification is: open water: blue; grease ice: gray; pancake and young (gray-white) ice: yellow; deformed first-year ice: red; multiyear ice: green; and undeformed first-year ice: violet. Source: Sandven et al. 1999.

#### 8.7.2.2 ZONE B: THE SMALL FLOE AREA

This zone is characterized by small floes, typically 10–100 m in size, that have been broken up by surface waves penetrating from open ocean into the ice pack. The width of the zone depends on the intensity of the wave field on preceding days. During the SIZEX experiment the zone was 20–30-km wide and was clearly identified in the SAR images as a more uniform zone between the open ocean and the interior of the ice pack (Figure 8-14a). The dominant ice type is rough first-year ice 2–3-m thick with backscatter values ranging from -10 to -6.5 dB. These values are significantly higher than for the undeformed first-year ice in Zone A due to the increased surface roughness. This surface roughness is caused by the

edges and ridges of the numerous small floes that cannot be identified in the SAR images. During the experiment the ice concentration was generally high (> 95%). Open water or thin ice between the floes had typical horizontal dimensions of 1–10 m, which could not be observed in the SAR images (Figure 8-15).

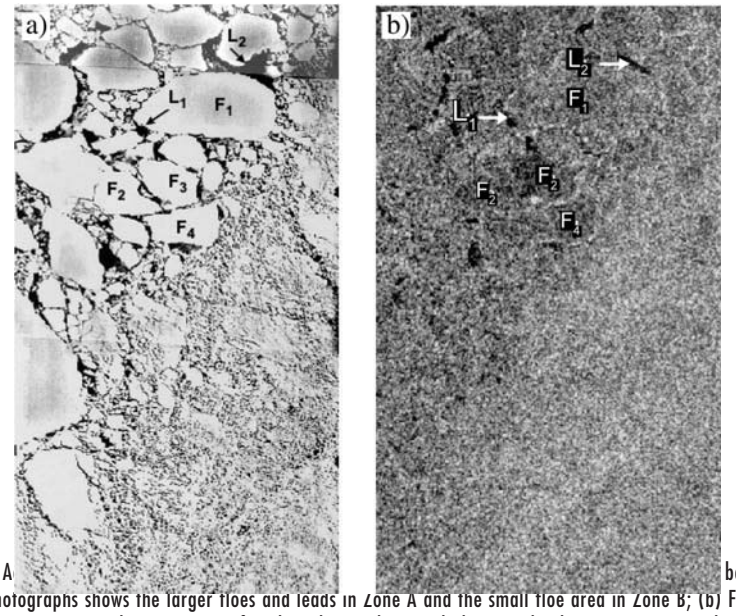


Figure 8-15 (a) A between Zones A and B. The photographs shows the larger floes and leads in Zone A and the small floe area in Zone B; (b) Full-resolution ERS-1 SAR subimage covering the same area of 14 by 7 km as the aerial photograph. The SAR image can identify the main leads between the large floes in Zone A, but direct floe identification is difficult even for the larger floes. In Zone B the SAR signature is very homogeneous and detection of features is very difficult. Source: Sandven et al., 1997.

Multiyear floes, which drift southwards with the East-Spitzbergen Current, could also occur in this zone. Similar to the first-year floes the multiyear floes tended to break up due to the wave field. The SAR signature of small multiyear floes was similar to that of surrounding first-year floes. Drifting icebergs with a horizontal scale of 100 m and a draft of 5–8 m were observed frequently in the zone, but their SAR signature even in full-resolution images was diffuse. Reliable observations of these icebergs could not be made by the ERS-1 SAR because the icebergs were embedded in first-year ice of nearly 100% concentration. The Wackerman classification method could mainly identify one ice type—denoted deformed first-year ice—and a few steps of young ice.

#### 8.7.2.3 ZONE C: THE AREA OF ICE FORMATION

Most of the ice in the Barents Sea is formed locally as the ice edge advances southwards during the freezing season. In the experiment the areas of ice formation were mapped by SAR images and documented by *in situ* observations. The first stage in ice formation is grease ice, which dampens out the short surface waves and causes low radar return signals. This ice had the lowest backscatter of all ice types, ranging from -24 to -14 dB. After 1–2 days of freezing the grease ice starts to form pancake ice with characteristic edges that cause high radar return, typically above -7.0 dB. As the pancake ice grows thicker during the winter it forms 1–2-m thick first-year ice. The ice in this zone is constantly exposed to surface waves and is therefore characterized by a rough surface. Grease ice and calm water (wind speed below 3 m/s) can have overlapping backscatter values, which make the inter-

pretation of the SAR images ambiguous; however no wind speeds below 3 m/s were observed in the experiment. Open water in the SAR images had higher backscatter than any of the observed ice types, from -4.5 to -3.0 dB. This region is the most difficult to classify because the backscatter varies rapidly between the various stages in new ice formation. Ambiguities occur between open water and some ice classes, in particular pancake/young ice, which are both characterized by high backscatter. There are also ambiguities and misclassification between pancake/young ice and deformed first-year ice. Improved ice classification in this region will require fully polarized images and possibly also multichannel SAR data.

#### 8.7.2.4 SUMMER CONDITIONS

The classification into three zones suggested for winter conditions would not be valid in summer, due to the higher temperature and the presence of melt water and wet snow. Zone C with ice formation would be absent. Zones A and B would be detectable, but the discrimination between different ice types becomes less significant. Because of wet snow and melt water on top of the ice, the SAR backscatter values from multiyear floes is reduced compared to the winter situation and becomes similar to the signature for first-year ice. It is therefore difficult to separate the two ice types based solely on backscatter levels (Johannessen et al. 1992). Thin ice types such as grease, pancake and young ice are usually not found in the summer.

The results from SIZEX 92 showed that the C-band VV-polarized ERS SAR could identify:

- 3–4-m thick multiyear ice floes, which originate from the Arctic Ocean north of Svalbard
- Refrozen leads with smooth thin ice
- Consolidated first-year ice 2–3-m thick, which is formed between multiyear floes in the interior of the ice pack during the winter
- Rough ice in leads, ridges and rubble fields
- First-year ice 2–3 m thick in a 20–30-km wide zone inside the ice edge broken up in typically 10–50-m large floes due to wave action (the floes in this zone are difficult to identify in the SAR images, but the overall zone can be recognized by a uniform bright signature)
- New ice formed outside the ice edge (grease ice and pancake ice)

The most difficult factor was the variable backscatter from open water due to wind speed. Ice classification algorithms have been applied to the SAR images from the SIZEX experiment, and the results from use of the Wackerman algorithm are shown in Figure 8-14b (Sandven et al. 1999). Such classifications will normally result in ambiguities, because different ice types can have similar SAR signatures. Also open water can have similar signature to some of the ice types, in particular pancake ice and ice with rough surface. In order to improve the algorithm for ice type determination and thus also for the ice edge detection and ice concentration estimation, it is necessary to know the open water signature as a function of wind speed, and to use the wind speed as an input parameter in the algorithms. With dual polarization data, as provided by *ENVISAT*, it is envisaged the polarization ratio should improve the discrimination between ice and open water (Flett 2004).

### 8.7.3 Radarsat Geophysical Processing System (RGPS)

The RGPS system was developed to improve understanding of sea ice interaction with the atmosphere and ocean in the polar regions and its impact on global climate (Kwok 1998). The RGPS system was designed to handle large amounts of RADARSAT ScanSAR data covering the whole Arctic Ocean, which started being produced in November 1996. The RGPS contains algorithms for transformation of radar backscatter data into geophysical parameters. The analysis tools provide consistent processing of data allowing comparisons to be made over wide spatial and temporal scales. The RGPS produces nearly complete ScanSAR Wide B mode coverage of the whole Arctic Ocean every six days (Figure 8-16).

The image production takes place at the Alaska SAR Facility. About 6,400 scenes are handled per year, corresponding to about 20 scenes per day. The radiometry and geometry of the images are controlled. From the sequence of SAR images, Lagrangian ice motion (Kwok et al. 1990) is determined by following the drift in deformation cells, which are initially 5 by 5 km. An operator inspects the ice drift estimates, which can be time consuming depending on the amount of deformation. For each cell the formation and aging of new ice, as well as deformation (ridge formation) during the freezing season, is followed in the time series of images. This allows determination of various stages in new and young ice. The discrimination between multiyear and first-year ice area is done by image classification. The age distribution of young ice can be converted to a thickness distribution using a simple empirical relation between accumulated freezing days and thickness (Figure 8-17).

Alternatively, a more complicated thermodynamic model can be used (Kwok et al. 1995). The RGPS can therefore be used to estimate the thickness distribution of ice volume produced by openings and closings of the ice cover since the beginning of the freezing season. This means that ice volume of the seasonal ice cover can be determined (Kwok and Cunningham 2002). To account for the ridged areas of unknown thickness, a separate category called “area of first-year (FY) ridges” is maintained in the RGPS record, allowing areas of ridged and undeformed ice to be followed through the freezing season. Other products from RGPS are maps of thin ice categories and maps of various Linear Kinematics Features (LKFs) derived from the ice drift vectors (Figure 8-18). The LKFs include long, narrow features whether or not they contain open water, new ice, nilas, young ice, first-year ice, rafted ice or ridged ice. Locally, they can be created by divergence, convergence, shear, or a combination of these. Examples of LKFs and other RGPS products can be found at http://www-radar.jpl.nasa.gov/rgps/radarsat.html. Validation of the RGPS products is a continuous activity. For the Lagrangian ice drift estimates, buoy drift data from the International Arctic Buoy Programme (IABP) are used.

### 8.7.4 Joint SAR and SLR Ice Studies in the Northern Sea Route

The Northern Sea Route (NSR), which is the sailing route along the northern coast of Russia from the Barents Sea to the Bering Strait, is the longest ice navigation route in the world. In the summer season (July–November), when major parts of the route are ice-free, navigation is possible along the whole route. Winter navigation is limited to the western part between the Murmansk and Yenisei river (Figure 8-19). In August–September 1997, the first demonstration of RADARSAT data for ice observation and navigation support in the eastern Kara Sea and Laptev Sea during summer was performed by the Nansen Centre in cooperation with the Murmansk Shipping Company’s nuclear icebreaker (N/I) *Sovetsky Soyuz* (Sandven et al. 2001).

In the late winter of 1998, a more extensive demonstration was carried out in the western part of the NSR (Alexandrov et al. 2000). During another expedition with N/I *Sovetsky*


Figure 8-16 Example of RADARSAT ScanSAR mosaic produced by the RADARSAT Geophysical Processor System, covering the major part of the Arctic Ocean. The mosaics are built up over a period of three days and are repeated every six days. Courtesy: R. Kwok.

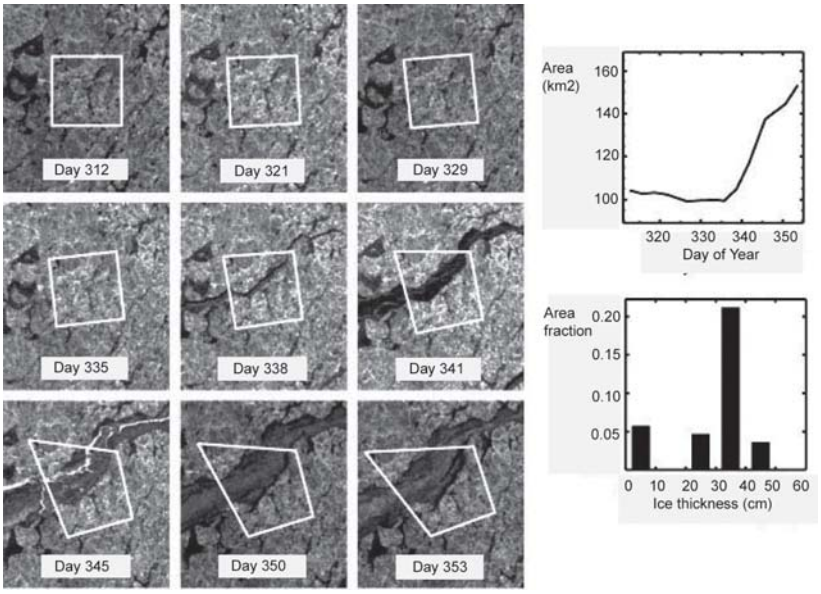


Figure 8-17 A time sequence of nine ScanSAR images following the drift and deformation of a unit cell over periods of 3–9 days. The unit cell is initially 100 km$^2$ but grows to about 150 km$^2$ towards the end of the period due to the formation of a large lead in the center of the image. The volume of new ice formation in the cell is estimated form the thickness distribution of ice thinner than 0.50 m at the end of the period. Courtesy: R. Kwok.

*Soyuz*, several Side-Looking Radar (SLR) images from the *Okean* satellite were obtained for the same areas as the RADARSAT ScanSAR images. Figures 8-20 and 8-21 show the two types of radar images simultaneously covering the eastern part of the Barents Sea, including the Pechora Sea and the Kara Gate. The images were obtained on 23 April 1998 and show in general the same ice features but with different resolution—250 m for the SAR image and about 1.5 km for the SLR image. The differences in resolution and imaging techniques result in a much more blurred and less detailed image provided by the SLR system compared to the SAR system. Radar wavelength is 3.2 cm (X-band) for the SLR and 5.6 cm (C-band) for the SAR, while polarization is VV for SLR and HH for SAR. Incidence angle ranges from 20° to 50° for both systems. The gray-scale of the two images is arbitrarily chosen to enhance the contrasts between the darker and brighter parts of the images. A quantitative comparison of absolute backscatter (sigma-0) requires calibrated images, which were not available for the study. The comparison could therefore only be done qualitatively.

Although the SLR images do not show the same details of the ice cover as the SAR images, they are useful to distinguish between young and FY ice, multiyear (MY) ice, and open water, and to identify wide fractures in the ice cover. Many navigationally important details however, such as narrow fractures and areas with ridged ice, cannot be identified in the SLR images. For example, the pattern of ridges observed in the SAR image east of Novaya Zemlya cannot be seen in the SLR image.

Both images show the gray-white ice of the coastal polynya on the western side of Novaya Zemlya as brighter signatures (area labeled *a* in the SAR image) compared to the thicker FY ice further north and west. A southward extension of the polynya into the Pechora Sea and towards the Kara gate is also well identified in both images as a bright feature (*b*). Both images showed that rough FY ice in the Pechora Sea, including a tongue of this ice intruding through the Kara Gate (*c*), were significantly brighter than level FY ice (*d*) observed east of Novaya Zemlya and the large dark FY floes north of about 75°N (*e*). Also the bright areas of young ice between the FY floes in this region (*f*) were evident in both images. Between 73° and 75°N small leads of open water, oriented nearly in a north-south direction, were clearly seen as dark stripes in the SAR image (*g*). The largest of these leads was also observable in the SLR image. In the same area there were some very well-defined bright line features in the SLR image that were oriented in a northeasterly direction. These bright lines, which we interpreted to be gray ice, were less pronounced in the SAR image, suggesting that VV-polarization responds stronger to this ice type than HH-polarization (Alexandrov et al. 2000).

The SAR ice navigation experiment with *Sovetsky Soyuz* showed that RADARSAT ScanSAR images can be very useful for navigation support in difficult ice conditions, such as those occurring in the Kara Sea region in April 1998. The analysis of the SAR images carried out after the experiment, supported by *in situ* observations, showed that the major navigationally important sea ice parameters could be identified in these images, such ice types, level and ridged FY ice, fractures, leads and polynyas. The ScanSAR signatures of the major ice types and features observed in the Kara Sea region have been described and to some extent verified by *in situ* observations from the icebreakers.

SLR images from satellites have been used for ice monitoring in the Russian Arctic since the 1980s, and SLR mosaics, as shown in Figure 8-22, can cover the ice areas every week in the winter period. The images have not been used in the summer season because the images have poor capability for discriminating ice from water and multiyear ice from first-year ice in the melt season. The main provider of SLR images is the Research Center for Operative Earth Monitoring (NTs OMZ) in Moscow.

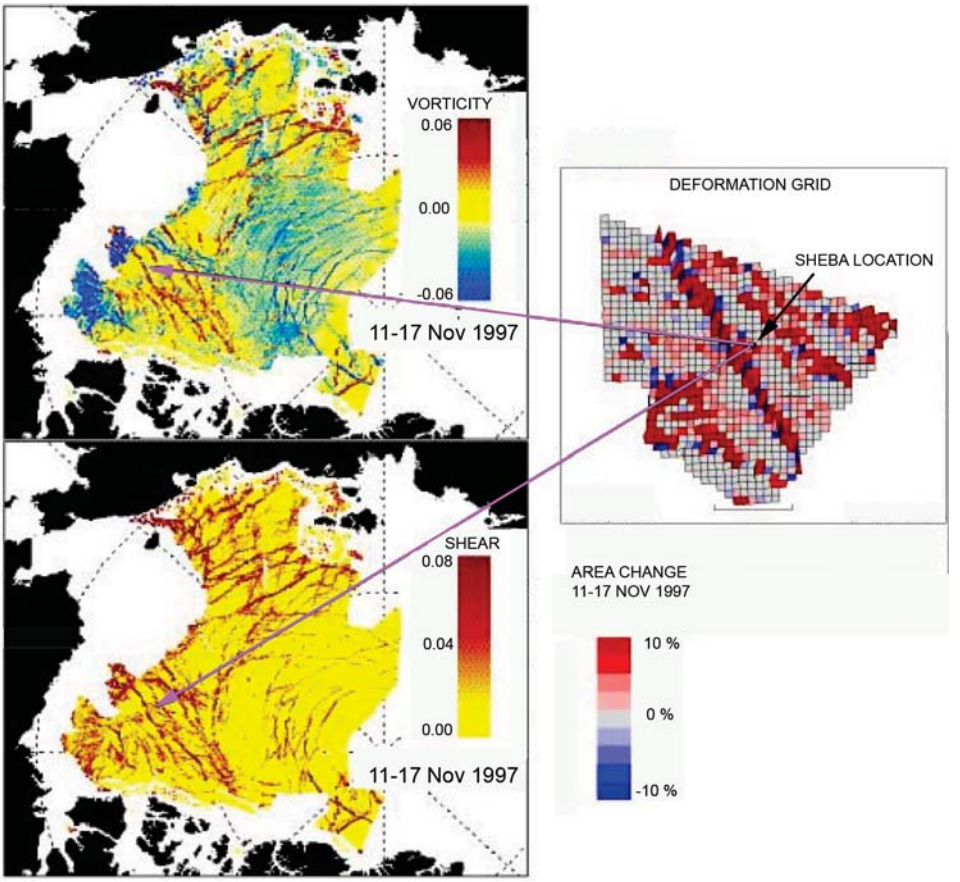


Figure 8-18 Maps of vorticity and shear are other examples of RGPS products derived for the velocity fields. Divergence, vorticity and shear are example of Linear Kinematics Features, illustrating long narrow features that often extend over large distances. Courtesy: R. Kwok.

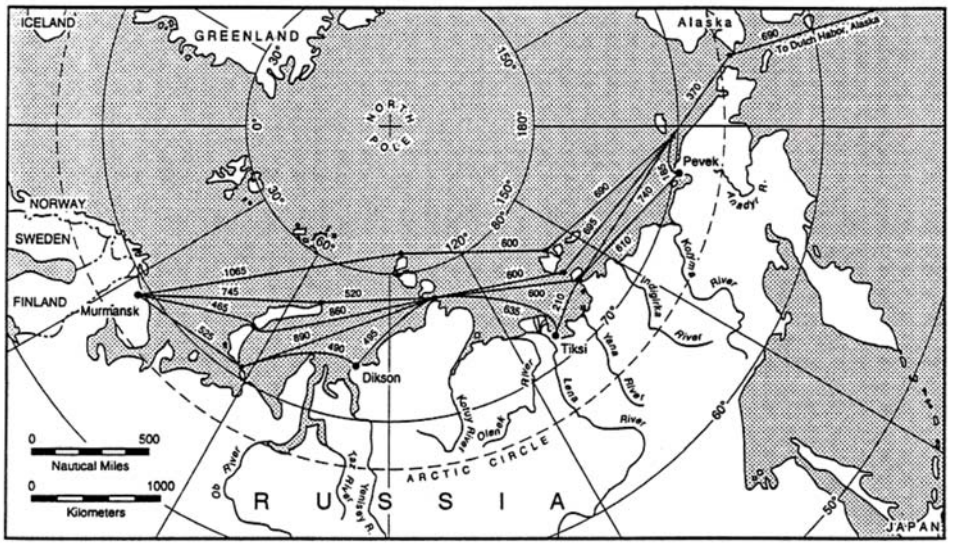


Figure 8-19 Map of the main sailing routes in the Russian Arctic, with approximate distances in nautical miles, of the various route segments between Murmansk and Dutch Harbour. Source: Mulherin 1996.

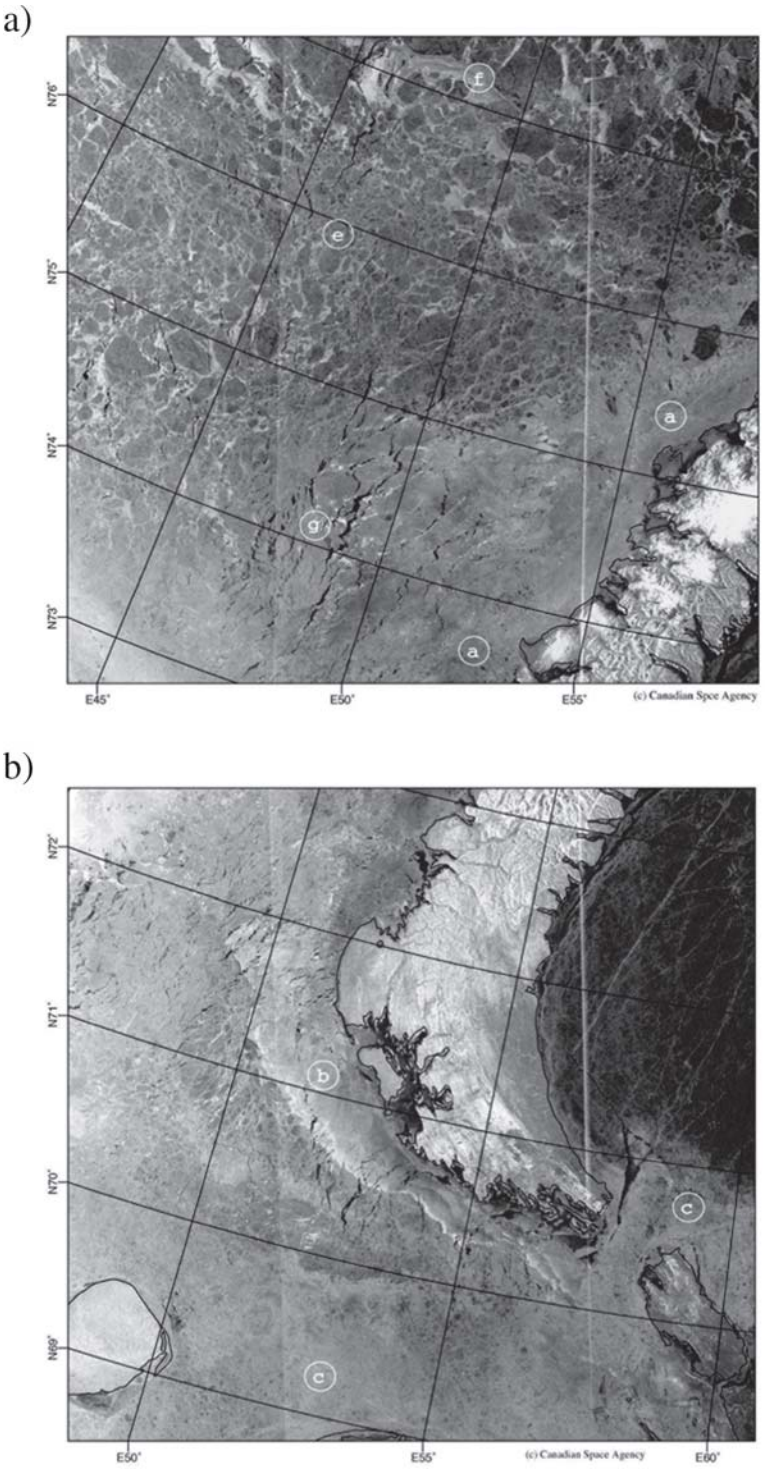


Figure 8-20 Two consecutive RADARSAT ScanSAR sea ice images from the area around Novaya Zemlya, obtained in a field expedition with N/I Sovetsky Soyuz in April 1998 during the ARCDEV project. The labels indicate the major ice types found in the images. Source: Alexandrov et al. 2000.

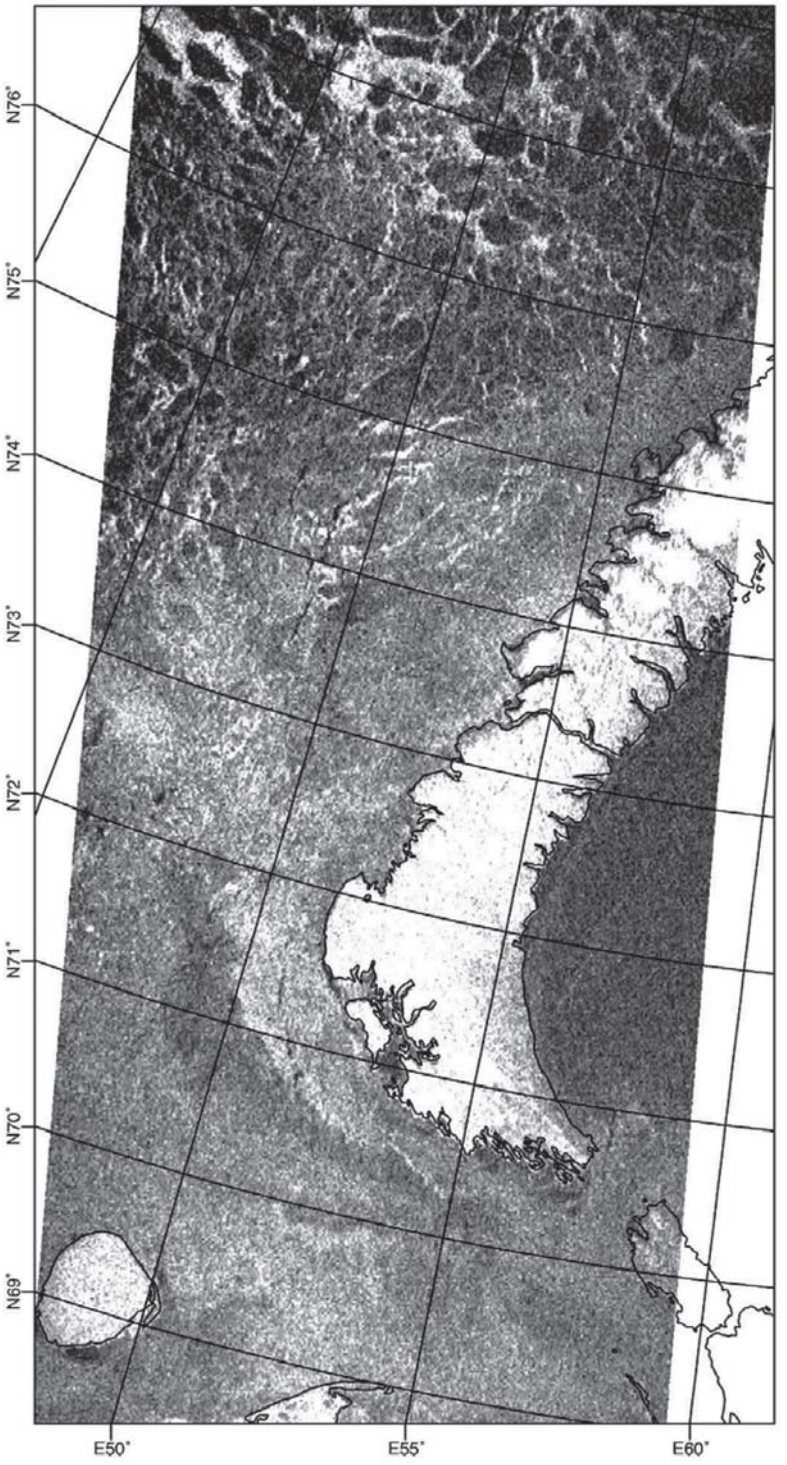


Figure 8-21 Okean SLR image obtained simultaneously with the RADARSAT images in Figure 8-22. Source: Alexandrov et al. 2000.

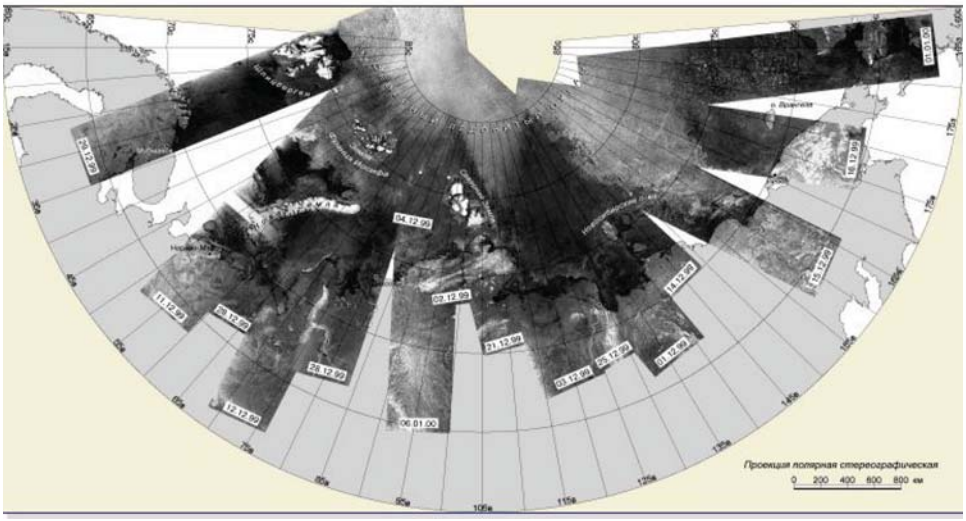


Figure 8-22 Example of Okean SLR mosaic of the Russian Arctic obtained in December 1999. The SLR mosaic shows clearly multiyear ice, first-year ice and open water areas. Courtesy: NTs OMZ.

### 8.7.5 Scatterometer Observations of Sea Ice

Spaceborne scatterometers have been in operation for more than a decade, providing continuous synoptic microwave coverage of the whole Earth. They have proven to be useful for observation of sea ice and many other marine and terrestrial parameters, although their prime objective is to measure ocean surface winds (Long et al. 2001). A scatterometer transmits radar pulses and receives backscattered energy in the same way as the SAR, but is designed to give lower spatial resolution data from a range of azimuths, thereby giving wind direction. Compared to SAR, the main benefit is the wide-swath coverage that allows daily observations of sea ice backscatter both in the Arctic and Antarctic, while the disadvantage is the much lower spatial resolution, generally 25–50 km, over incidence angles ranging from 20–55°. Sea ice extent has been readily identified by several spaceborne scatterometers over the last decade, with *QuikSCAT* as the most important because it has been in operation since 1999 (e. g. Gohin and Cavanié 1995; Ezraty and Cavanié 1999; Remund and Long 1999). Sigma-nought image mosaics are produced in near-real-time for both the Arctic and Antarctic (Figure 8-23) using the QuikSCAT Ku-band SeaWinds instrument, which has been the most important scatterometer in operation since 1999.

Algorithms to retrieve ice edge and low ice concentration from *QuikSCAT* are under development (e.g., Haarpaintner et al. 2004). Furthermore, ice velocity fields and ice-type classification can also be derived from the scatterometer ice maps (Figure 8-24). Ice velocity fields are important for estimating heat flux between the ocean and atmosphere, as well as the sea ice mass balance through estimates of ice deformation and growth. Motion fields have been derived using scatterometer data with algorithms based on wavelet analysis (Liu et al. 1999), and ice motion from scatterometer data has been validated by Zhao et al. (2002). Several new scatterometer missions are planned in the future, allowing sea ice monitoring by scatterometers to be an operational service. Presently, scatterometer sea ice products are provided by NOAA NESDIS (http://manati.orbit.nesdis.noaa.gov/cgi-bin/qscat_ice.pl) and CERSAT at IFREMER (http://www.ifremer.fr/cersat/en/data/data.htm). The sea ice products delivered by the EUMETSAT Ocean and Sea Ice Satellite Application Facility (O&SI SAF) make use of scatterometer, SSMI and NOAA AVHRR data (Breivik et al. 2001).

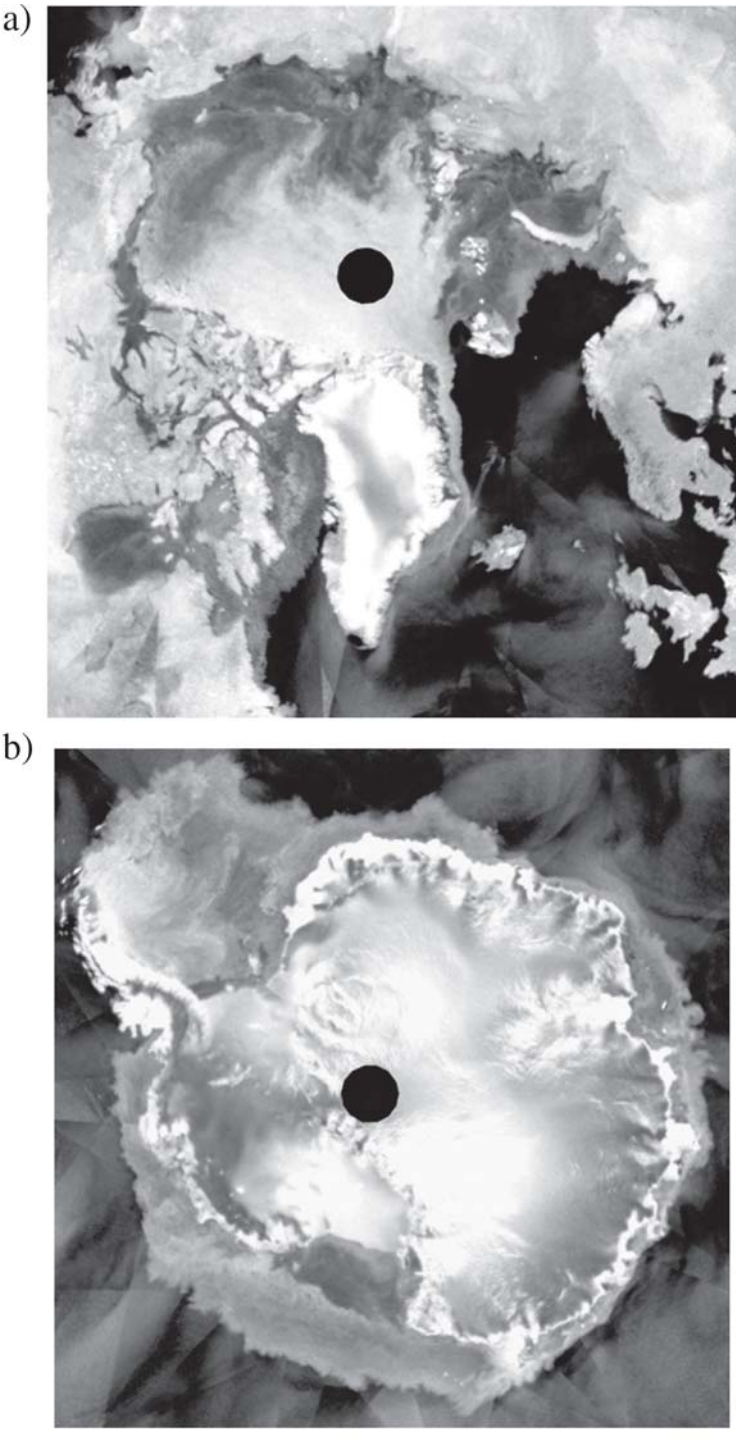


Figure 8-23 Scatterometer sigma-nought mosaics showing sea ice areas in Arctic (a) and Antarctic (b) obtained from *QuikSCAT* on 23 April 2004.

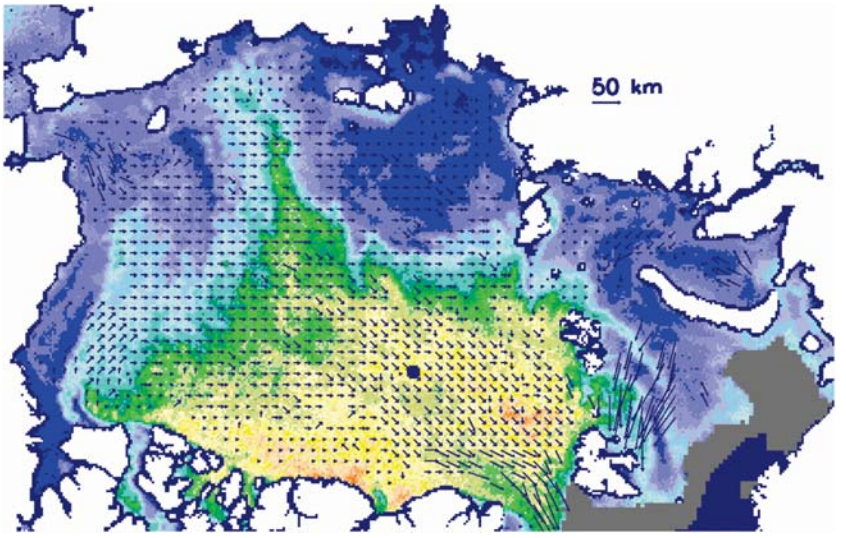


Figure 8-24 Example of IFREMER scatterometer sea ice product showing backscatter values in colors where green/yellow/red represents multiyear ice and light/dark blue represents first-year ice. Ice drift vectors represent three-day intervals. Courtesy: R. Ezraty.

## 8.8 NEW DEVELOPMENTS IN SEA ICE REMOTE SENSING

A new generation of microwave radiometers is represented by the Advanced Microwave Scanning Radiometer – EOS (AMSR-E), which has been developed jointly by NASA and NASDA and was launched on the EOS *Aqua* satellite in May 2002. AMSR-E provides higher resolution footprints, down to 6 by 4 km for the 89-GHz channel (Kramer 2002 and http://wwwghcc.msfc.nasa.gov/AMSR/). The algorithms for retrieving sea ice concentration from AMSR-E data have been reviewed by Cavalieri and Comiso (2000), showing how existing algorithms have been adapted to the AMSR-E data. A validation program for the AMSR-E sea ice products is defined for both the Arctic and Antarctic. Examples of sea ice concentration maps derived from the AMSR-E data are available at http://www.seaice.de, provided by Institute of Environmental Physics at University of Bremen. The improvement from the 15-km resolution SSM/I-based ice maps to the 6-km resolution AMSR-E maps is demonstrated in Figure 8-25. Preliminary comparisons show that there is a significant improvement in the quality of the ice maps from the AMSR-E data, especially in the ice edge regions and along coastlines.

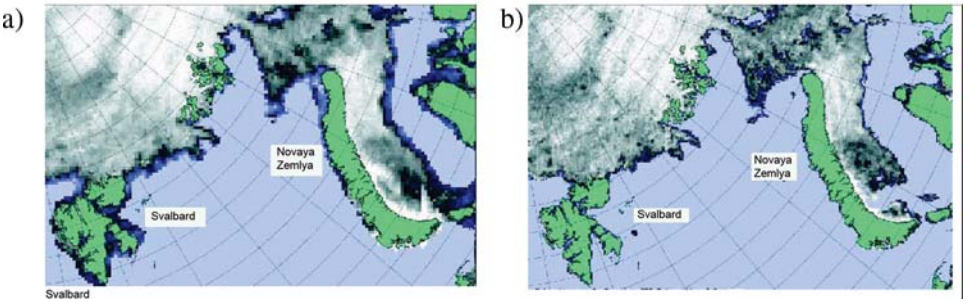


Figure 8-25 Comparison of ice concentration from (a) SSMI and (b) AMSR-E data for the Barents Sea area using the ARTIST algorithm by Kaleschke et al. (2001). The improved resolution of the AMSR-E data reduces the land effects and increases the sharpness of the ice edge. Courtesy: G. Heygster.

A method for ice thickness retrieval from radar altimeter data has been developed by Laxon et al (2003) based on ERS altimeter data that have been obtained up to 81.5°N since 1992. The method is based on separation of the signals from sea ice floes and open water or thin ice in leads, and then calculation of freeboard, which is translated into thickness based on climatological estimates of snow cover and ice density. The ice thickness estimates are the result of averaging all the data to monthly mean values, typically on 100 by 100-km grids. ERS-retrieved thicknesses have been validated by comparison with submarine ice draft measurements (Figure 8-26). These methods allow retrieval of ice thickness above 1 m and exclude the marginal ice zone.

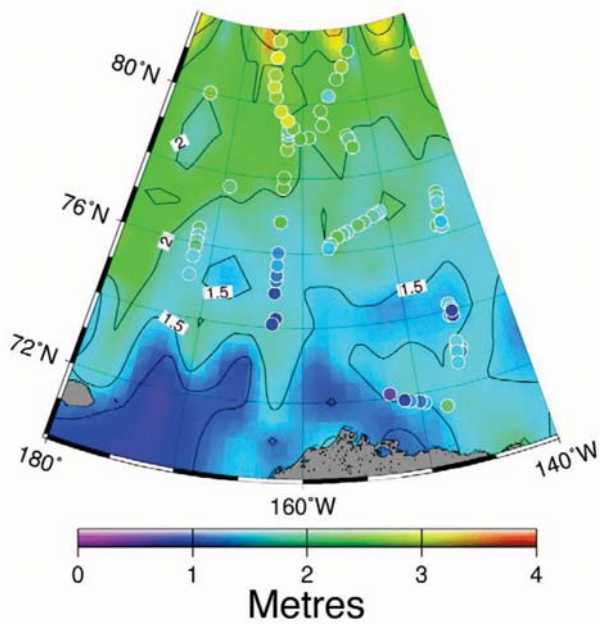


Figure 8-26 Sea ice thickness derived from ERS radar altimeter data in the Beaufort Sea. The circles indicate ice thickness measurements from submarine cruises used for validation of the altimeter estimates. Courtesy: S. Laxon.

ENVISAT ASAR has dual-polarization capabilities, and the Alternating Polarization (AP) mode allows acquisition of three dual-polarization combinations: HH and HV, VV and VH, or HH and VV. Initial results from ASAR AP data suggest that cross-polarization will improve the potential for distinguishing ice from open water, which can sometimes be difficult with only HH or VV polarization. The sensor noise floor for the cross-polarization channel can be a limiting factor in observing ice types with low backscatter, such as for discrimination of thin, new ice and open water areas. Therefore, the co-polarization option (HH and VV) of the Alternating Polarization mode may be preferable, as research has shown that the co-polarization ratio may also be useful for discriminating ice from open water areas (Scheuchl et al. 2001; De Abreu et al. 2003). An example of discrimination between ice and water from ENVISAT AP mode is shown in Figure 8-27.

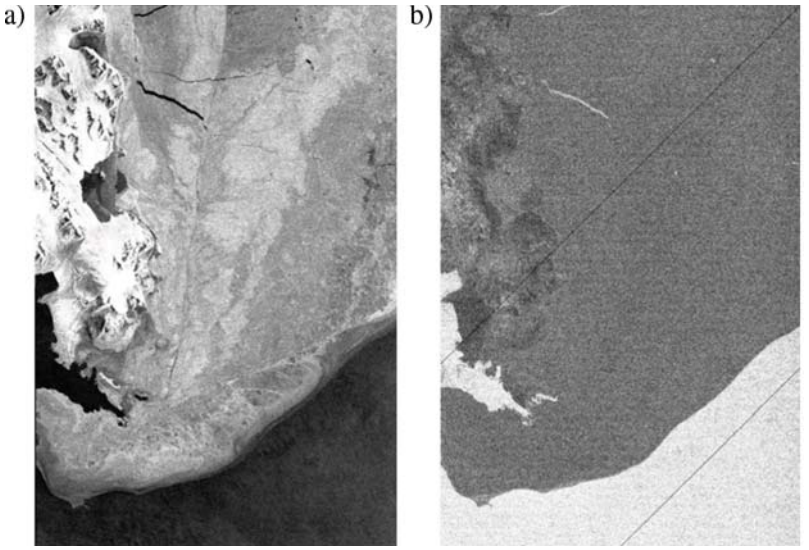


Figure 8-27 Example of ENVISAT Alternating polarization image with about a 100-km swath width in the Svalbard region showing (a) HH-polarization, and (b) polarization ratio (VV/HH) where the open water and sea ice is well discriminated.

Another advantage of cross-polarization images is for better detection of ridges and discrimination between MY and FY ice, as well as between level ice and deformed ice. Observations of C-band scatterometer measurements of Baltic sea ice from aircraft quantitatively illustrated that the backscatter contrast between level ice and ice ridges is larger at cross-polarization than co-polarization (Makynen and Hallikainen 1998). Multiyear versus first-year ice contrast is as high as 9 dB in the cross-polarization data, compared to less than 3 dB in the like-polarization channels. It is envisaged that cross-polarization ScanSAR data from *RADARSAT-2* will be an improvement over the current like-polarization case for detection of ice topography and structure. Other new spaceborne SAR systems will contribute to ice observation in the next few years, such as the L-band, polarimetric ALOS PALSAR, and the X- and L-band polarimetric *TerraSAR*. The possibilities to have SAR data in three frequencies (X-, C- and L-band) in combination with polarimetric capabilities offer unique opportunities to extract more information about various ice classes ands ice features from SAR. An example of a three-frequency composite (P-, C- and L-band) from airborne SAR is shown in Figure 8-28.

ENVISAT ASAR Global Mode offers a new opportunity to observe and monitor most of the Arctic and Antarctic sea ice, since this is a default mode of operation that is used when no other modes are requested. This low-energy mode provides image strips with 500-m pixel size, swath width of 450 km, and 1-km resolution. The images require no pre-ordering and are available in near-real-time from a server at ESA. This is a very convenient capability that makes it suitable for operational monitoring. However, analysis of these images has not yet started so it is not yet clear which products can be derived from the Global Mode.

Sea ice measurements from space are now in a very interesting development phase where high-resolution global sea ice data from SAR is feasible and use of the RGPS can provide more details about the dynamic and thermodynamic information. When ice topography and thickness measurements from ICESat are combined with SAR, a new era in ice observation will start. Ice volumes and fluxes will be determined more accurately, which will improve ice modeling and forecasting. Assimilation of ice concentration from SSM/I data in coupled ice-ocean models has started (e.g., Lisæter et al. 2003). Ice drift and thick-

ness will be added when there is sufficient coverage across the Arctic Ocean. It is envisaged that all the major sea ice parameters will become available from space data within the next decade, with SAR and altimeters playing key roles. This will contribute to improved description and modeling of sea ice from basin-wide scales down to regional and local scales.

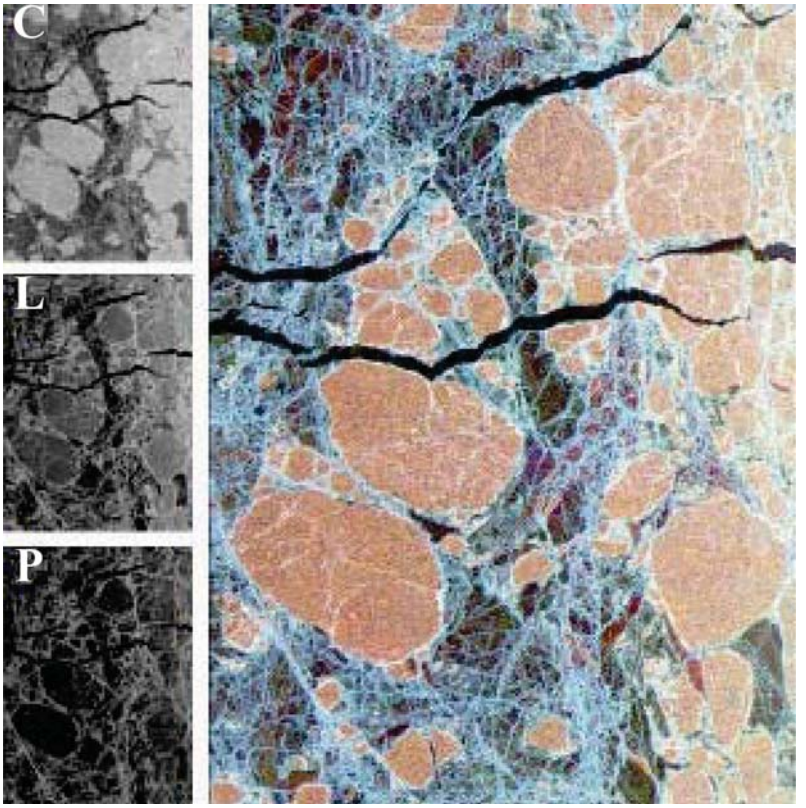


Figure 8-28 Multi-frequency JPL AirSAR data of sea ice from the Beaufort Sea acquired in 1988. Total Power images for C, L, and P bands and false color composite (Red: C-band; Green: L-band; Blue: P-band) illustrating the visual synergy of the three frequencies when combined. After Flett 2004.

## 8.9 ACKNOWLEDGEMENT

We would like to thank our many colleagues, mentioned in the reference list, for valuable contributions to this article.

# REFERENCES

Alexandrov, V. Yu., S. Sandven, O. M. Johannessen, Ø. Dalen, and L. H. Pettersson. 2000. Winter navigation in the Northern Sea Route. *Polar Record* 36, no. 199:333–342.

Bertoia, C., M. Manore, H. Steen Andersen, C. O'Connors, K. Q. Hansen, and C. Evanego. 2004. Synthetic aperture radar for operational ice observation and analysis. Chapter 20, pages 417–442 in *Synthetic Aperture Radar. Marine User's Manual*, edited by C. R. Jackson and J. R. Apel. Washington, D.C.: National Oceanic and Atmospheric Administration.

Bjørgo, E., O. M. Johannessen, and M. W. Miles. 1997. Analysis of merged SMMR/SSMI time series of Arctic and Antarctic sea ice parameters. *Geophys. Res. Lett.* 24:413–416.

Breivik, L.-A., S. Eastwood, Ø. Godøy, H. Schyberg, S. Andersen, and R. Tonboe. 2001. Sea ice products for EUMETSAT satellite application facility. *Can. J. Rem. Sens*. 27, no. 5:403–410.

Campbell, W. J. 1973. NASA remote sensing of sea ice AIDJEX. *Proceedings of the World Meteorological Organization Technical Conference*, Tokyo, Japan, WMO No. 350, 55–56.

Caneva, N. 1992. *ERS-1 SAR Calibration.* Frascati, Italy: European Space Agency.

Carsey, F. D., ed. 1992. *Microwave Remote Sensing of Sea Ice*. AGU Geophysical Monograph 68. Washington, D.C.: American Geophysical Union.

Cavalieri, D. J. and J. C. Comiso. 2000. *Algorithm Theoretical Basis Document for the AMSR-E Sea Ice Algorithm*, revised December 1. Landover, Md.: Goddard Space Flight Center.

Cavalieri, D. J., P. Gloersen, and W. J. Campbell. 1984. Determination of sea-ice parameters with the NIMBUS-7 SMMR. *J. Geophys. Res.* 89:5355–5369.

Cavalieri, D. J., J. P. Crawford, M. R. Drinkwater, D. T. Eppler, L. D. Farmer, R. R. Jentz, and C. C. Wackerman. 1991. Aircraft active and passive microwave validation of sea ice from the Defense Meteorological Satellite Program Special Sensor Microwave Imager. *J. Geophys. Res*. 96:21989–22008.

Cavalieri, D. J., P. Gloersen, C. E. Parkinson, H. J. Zwally, and J. C. Comiso. 1997. Observed hemispheric asymmetry in global sea ice changes. *Science* 278:1104–1106.

Comiso, J. C. 1983. Sea ice emissivities from satellite passive microwave and infrared observations. *J. Geophys. Res*. 88:7686–7704.

———. 1995. SSM/I ice concentrations using the bootstrap algorithm. *NASA Tech. Rep. 1380*. Greenbelt, Md.: NASA Goddard Space Flight Center.

Comiso, J. C., D. J. Cavalieri, C. L. Parkinson, and P. Gloersen. 1997. Passive microwave algorithms for sea ice concentration – A comparison of two techniques. *Rem. Sens. Environ*. 60:357–384.

De Abreu, R., D. Flett, B. Scheuchl, and B. Ramsay. 2003. Operational sea ice monitoring with RADARSAT-2 – A glimpse into the future. *Proceedings, IGARSS 2003*, July 21–25, Toulouse, France.

Eppler, D. T., L. D. Farmer, A. W. Lohanick, M. R. Anderson, D. J. Cavalieri, J. Comiso, P. Gloersen, C. Garrety, T. C. Grenfell, M. Hallikainen, J. A. Maslanik, C. Matzler, R. A. Melloh, I. Rubinstein, and C. T. Swift. 1992. Passive microwave signatures of sea ice. Chapter 4, pages 47–71 in *Microwave Remote Sensing of Sea Ice*, edited by F. Carsey. AGU Geophysical Monograph 68. Washington, D.C.: American Geophysical Union.

ESA. 2002. *ASAR Product Handbook*. Issue 1.0. Frascati, Italy: European Space Agency.

Ezraty, R. and A. Cavanié. 1999. Construction and evaluation of 12.5 km grid NSCAT backscatter maps of Arctic Sea ice. *IEEE Trans. Geosc. and Rem. Sensing* 37, no. 3.

Flett, D. G. 2004. Operational use of SAR at the Canadian Ice Service: Present operations and a look to the future. *ESA Proceedings of the Second Workshop on Coastal and Marine Applications of SAR*, 12–15 September 2003, Svalbard, Norway (SP-565, 2004), 183–198.

Gloersen, P., W. J. Campbell, D. J. Cavalieri, J. C. Comiso, C. L. Parkinson, and H. J. Zwally. 1992. Arctic and Antarctic sea ice, 1978–1987. *Satellite Passive-Microwave Observations and Analysis*. NASA SP-511. Washington, D.C.: National Aeronautics and Space Administration.

Gohin, F. and A. Cavanié. 1995. A first try at identification of sea ice using the three beam scatterometer of ERS-1. *Int. J. Remote Sens*. 16:2031–2054.

Haarpaintner, J., R. T. Tonboe, D. G. Long, and M. L. VanWoert. 2004. Automatic detection and validity of sea ice edge: An application of enhanced resolution QuikScat/SeaWinds data. *IEEE Trans. Geosc. and Rem. Sensing Science* 42:1433–1444.

Hallikainen, M. and D. P. Winebrenner. 1992. The physical basis for sea ice remote sensing. Chapter 3, pages 29–46 in *Microwave Remote Sensing of Sea Ice*, edited by F. Carsey. AGU Geophysical Monograph 68. Washington, D.C.: American Geophysical Union.

Haykin, S., E. O. Lewis, R. K. Raney, and J. R. Rossiter. 1994. *Remote Sensing of Sea Ice and Icebergs*. Wiley Series in Remote Sensing. New York: John Wiley & Sons.

Jackson, C. R. and J. R. Apel, eds. 2004. *Synthetic Aperture Radar. Marine User's Manual.* Washington, D.C.: National Oceanic and Atmospheric Administration.

Johannessen, O. M., M. Miles, and E. Bjørgo. 1995. The Arctic's shrinking sea ice. *Nature* 376:126–127.

Johannessen, O. M., E. V. Shalina, and M. W. Miles. 1999. Satellite evidence for an Arctic sea ice cover in transformation. *Science* 286:1937–1939.

Johannessen, O. M., W. J. Campbell, R. Shuchman, S. Sandven, P. Gloersen, J. A. Johannessen, E. G. Josberger, and P. M. Haugan. 1992. Microwave study programs of air-ice-ocean interactive processes in the seasonal ice zone of the Greenland and Barents seas. Chapter 13, pages 261–289 in *Microwave Remote Sensing of Sea Ice*, edited by F. Carsey. AGU Geophysical Monograph 68. Washington, D.C.: American Geophysical Union.

Johannessen, O. M., A. M. Volkov, L. P. Bobylev, V. D. Grischenko, S. Sandven, L. H. Pettersson, V. V. Melentyev, V. Asmus, O. E. Milekhin, V. A. Krovotyntsev, V. G. Smirnov, V. Yu. Alexandrov, G. Duchossois, V. Kozlov, G. Kohlhammer, and G. Solaas. 2000. ICEWATCH - Real-time sea ice monitoring of the Northern Sea Route using satellite radar (a Cooperative Earth Observation Project between the Russian and European Space Agencies). *Earth Observ. and Rem. Sens.* 16, no. 2:257– 268.

Johannessen, O. M., L. Bengtsson, M. W. Miles, S. I. Kuzmina, V. Semenov, G. V. Alekseev, A. P. Nagurny, V. F. Zakharov, L. P. Bobylev, L. H.Pettersson, K. Hasselmann, and H. P. Cattle. 2004. *Arctic Climate Change – Observed and Modelled Temperature and Sea Ice*. Pages 328–341 in Dynamic Meteorology and Oceanography, Tellus Series A, vol. 56A, no. 4. Stockholm: Swedish Geophysical Society.

Johannessen, O. M., V. Yu. Alexandrov, I. Ye. Frolov, S. Sandven, M. Miles, L. P. Bobylev, L. H. Pettersson, V. G. Smirnov, and E. U. Mironov. 2005. *Remote Sensing of Sea Ice in the Northern Sea Route: Studies and Applications*. Springer Praxis Books.

Kaleschke, L., G. Huygster, C. Lupkes, A. Bochert, J. Hartmann, J. Haarpaintner, and T. Vihma. 2001. SSM/I sea ice remote sensing for mesoscale ocean-atmosphere interaction analysis. *Can. J. Rem. Sens.* 27, no. 5:526–537.

Kern, S. 2001. A new algorithm to retrieve the sea ice concentration using weather-corrected 85 GHz SSM/I measurements. Ph. D. thesis, Dept. Physics Elect. Eng. Univ. Bremen, Bremen, Germany.

Kramer, H. J. 2002. *Observation of the Earth and Its Environment. Survey of Missions and Sensors.* 4th ed. Berlin and Heidelberg: Springer Verlag.

Kwok, R. 1998. The RADARSAT geophysical processor system. Pages 235–257 in *Analysis of SAR Data of the Polar Oceans*, edited by C. Tsatsoulis and R. Kwok. Berlin and Heidelberg: Springer Verlag.

Kwok, R. and G. F. Cunningham. 2002. Seasonal ice area and volume production of the Arctic Ocean: November 1996 through April 1997. *J. Geophys. Res.* 107, C10:8038–8055.

Kwok, R., J. C. Curlander, R. McConnell, and S. S. Pang. 1990. An ice motion tracking system at the Alaska SAR Facility. *IEEE J. Oceanic Eng.* 15:44–55.

Kwok, R., D. A. Rothrock, H. L. Stern, and G. F. Cunningham. 1995. Determination of ice age using Lagrangian observations of ice motion. *IEEE Trans. Geosci. Rem. Sens.* 33, no. 2:392–400.

Kwok, R., A. Schweiger, D. A. Rothrock, S. Pang, and C. Kottmeier. 1998. Sea ice motion from satellite passive microwave imagery assessed with ERS SAR and buoy motions. *J. Geophys. Res.* 103, C4:8191–8214.

Laxon, S., N. Peacock, and D. Smith. 2003. High interannual variability of sea ice thickness in the Arctic region. *Nature* 245:947–950.

Lensu, M., S. Heale, K. Riska, and P. Kujula. 1996. Ice environment and ship hull loading along the Northern Sea Route. *INSROP Working Paper No. 66*. Lysaker, Norway: International Northern Sea Route Programme.

Lisæter, K. A., J. Rosanova, and G. Evensen. 2003. Assimilation of ice concentration in a coupled ice–ocean model, using the Ensemble Kalman filter. *Ocean Dynamics* 53:368–388.

Liu, A. K. and D. J. Cavalieri. 1998. On sea ice drift from wavelet analysis of the Defense Meteorological Satellite Program (DMSP) Special Sensor Microwave Imager (SSM/I) data. *Int. J. Remote Sensing* 19: 415–1423.

Liu, A. K., Y. Zhao, and S. Y. Wu. 1999. Arctic sea ice drift from wavelet analysis of NSCAT and special sensor microwave imager data. *J. Geophys. Res.* 104:11529–11538.

Long, D. G., M. R. Drinkwater, B. Holt, S. Saatchi, and C. Bertoia. 2001. Global ice and land climate studies using scatterometer image data. *EOS, Transaction of the American Geophysical Union* 82, no. 43:503. Includes EOS Electronic Supplement: http://www.agu.org/eos_elec/010126e.html (last accessed Oct. 2005).

Makynen, M. and M. Hallikainen. 1998. C-Band backscattering signatures of Baltic sea ice. *Proceedings IGARSS'98*, Seattle, Washington, July 6–10.

Martin, T. and E. Augstein. 2000. Large-scale drift of Arctic Sea ice retrieved from passive microwave satellite data. *J. Geophys. Res*. 105, C4:8775–8788.

Mulherin, N. D. 1996. The Northern Sea Route. Its development and evolving state operations in the 1990s. *CRREL Report 96-3*. US Army Engineer District, Alaska. US Army Corps of Engineers.

Onstott, R. G. and R. A Shuchman. 2004. SAR measurements of sea ice. Chapter 3, pages 81–115 in *Synthetic Aperture Radar. Marine User's Manual*, edited by C. R. Jackson and J. R. Apel. Washington, D.C.: National Oceanic and Atmospheric Administration.

Parkinson, C. L., D. J. Cavalieri, P. Gloersen, H. J. Zwally, and J. C. Comiso. 1999. Arctic sea ice extents, areas and trends, 1978–1996. *J. Geophys. Res*. 104, C9:20837–20856.

Pettersson, L. H., S. Sandven, Ø. Dalen, V. V. Melentyev, and N. I. Babich. 1999. Satellite radar ice monitoring for ice navigation of the ARCDEV tanker convoy in the Kara Sea. *Proceedings of the 15th International Conference on Port and Ocean Engineering under Arctic Conditions*, Helsinki, Finland, 23–27 August, 141–153.

Remund, Q. P. and D. G. Long. 1999. Sea ice extent mapping using Ku-band scatterometer data. *J. Geophys. Res*. 104, C5:11515–11527.

Robinson, I. A. 2004. *Measuring the Oceans from Space*. Chichester, U.K.: Springer Praxis Publishing Ltd.

Rothrock, D. A., Y. Yu, and G. A. Maykut. 1999. Thinning of the Arctic sea-ice cover. *Geophys. Res. Lett*. 26:3469–3472.

Rubinstein, I. G., D. M. Nazarenko, and S. Tam. 1994. Passive microwave systems. Chapter 5, pages 177–257 in *Remote Sensing of Sea Ice and Icebergs*, edited by S. Haykin, E. O. Lewis, R. K. Raney, and J. R. Rossiter. Wiley Series in Remote Sensing. New York: John Wiley & Sons.

Sandven, S., O. M. Johannessen, M. W. Miles, L. H. Pettersson, and K. Kloster. 1999. Barents Sea seasonal ice zone features and processes from ERS-1 SAR: SIZEX92. *J. Geophys. Res*. 104, C7:15843–15857.

Sandven, S., Ø. Dalen, M. Lundhaug, K. Kloster, V.Y. Alexandrov, and L. V. Zaitsev. 2001. Sea ice investigations in the Laptev Sea area in late summer using SAR data. *Can. J. Rem. Sens*. 27, no. 5:502–516.

Sandven, S., K. Kloster, H. Tangen. T. S. Andreassen, H. Goodwin, and K. Partington. 2004. Sea ice mapping using ENVISAT ASAR wideswath images. *Proceedings of the Second Workshop on Coastal and Marine Applications of SAR*, 12–15 September 2003, Svalbard, Norway (SP-565, 2004), 161–168.

Scheuchl, B., R. Caves, I. Cumming, and G. Staples. 2001. Automated sea ice classification using spaceborne polarimetric SAR data. *Proceedings, IGARSS 2001*, Sydney, Australia, July 9–13.

Shuchman, R. A. and R. G. Onstott. 1990. Remote sensing of polar oceans. Chapter 3 in *Polar Oceanography, Part A Physical Science*, edited by W. O. Smith Jr. San Diego: Academic Press.

Smith, D. M. 1998. Recent increase in the length of the melt season of perennial Arctic sea ice. *Geophys. Res. Lett.* 25:655–658.

Steffen, K., J. Key, D. J. Cavalieri, J. Comiso, P. Gloersen, K. St. Germain, and I. Rubinstein. 1992. The estimation of geophysical parameters using passive microwave algorithms. Chapter 10, pages 201–231 in *Microwave Remote Sensing of Sea Ice*, edited by F. Carsey. AGU Geophysical Monograph 68. Washington, D.C.: American Geophysical Union.

Strogyn, A. 1971. Equations for calculating dielectric constant of saline water. *IEEE Trans. Microwave Theory Tech.* Vol. MTT-19:733–736.

Svendsen, E., C. Maetzler, and T. C. Grenfell. 1987. A model for retrieving total sea ice concentration from spaceborne dual-polarized passive microwave instrument operating near 90 Ghz. *Int. J. Rem. Sens.* 8, no. 10:1479–1487.

Svendsen, E. A., K. Kloster, B. A. Farrelly, O. M. Johannesen, J. A. Johannessen, W. J. Campbell, P. Gloersen, D. Cavalieri, and C. Matzler. 1983. Norwegian remote sensing experiment: Evaluation of the Nimbus 7 Scanning Multichannel Microwave Radiometer for sea ice research. *J. Geophys. Res.* 88, C5:2781–2791.

Swift, C. T. and D. J. Cavalieri. 1985. Passive microwave remote sensing for sea ice research. *EOS Trans. of Amer. Geophys. Union* 66:1210–1212.

Tsatsoulis, C. and R. Kwok, eds. 1998. *Analysis of SAR Data of the Polar Oceans*. Berlin and Heidelberg: Springer Verlag.

Ulaby, F. T., R. K. Moore, and A. K. Fung. 1982a. Real aperture side-looking airborne radars. Pages 562–629 in *Microwave Remote Sensing - Active and Passive: Volume II - Radar Remote Sensing and Surface Scattering and Emission Theory*. Reading, Mass.: Addison-Wesley Publishing Co.

———. 1982b. Synthetic aperture side-looking airborne radar systems. Pages 630–745 in *Microwave Remote Sensing - Active and Passive: Volume II - Radar Remote Sensing and Surface Scattering and Emission Theory*. Reading, Mass.: Addison-Wesley Publishing Co.

Wadhams, P. 1994. Sea ice thickness changes and their relation to climate change. Pages 337–362 in *The Polar Oceans and Their Role in Shaping the Global Environment: Nansen Centennial Volume*. American Geophysical Union Monograph 85. Washington, D.C.: American Geophysical Union.

WMO. 2004. *Ice Chart Colour Standard.* WMO/TD-No. 1215. JCOMM Technical Report No. 24. http://www.wmo.ch/web/aom/marprog/index.htm (last accessed Oct. 2005).

Zhao, Y., A. K. Liu, and D. G. Long. 2002. Validation of sea ice motion from QuikSCAT with those from SSM/I and buoy. *IEEE Transac. on Geosci. and Rem. Sens. Vol*. 40, no. 6:1241–1246.

Zwally, H. J., J. Comiso, C. L. Parkinson, W. J. Campbell, F. D. Carsey, and P. Gloersen. 1983. Antarctic sea ice, 1973–1976. *Satellite Passive Microwave Observations*, NASA SP-459.

Zwally, H. J., B. Schutz, W. Abdalati, J. Abshire, C. Bentley, A. Brenner, J. Bufton, J. Dezio, D. Hancock, D. Harding, T. Herring, B. Minster, K. Quinn, S. Palm, J. Spinhirne, and R. Thomas. 2002. ICESat's laser measurements of polar ice, atmosphere, ocean, and land. *J. Geodynamics* 34:405–445. <http://icesat.gsfc.nasa.gov>(last accessed October 2002).